7

Permeation control through stimuli-responsive polymer membrane prepared by plasma and radiation grafting techniques

YOUNG MOO LEE AND JIN KIE SHIM

7.1 Introduction

Stimuli-sensitive polymer drug delivery, especially using temperature and pH-sensitive hydrogels and polymeric membranes, may be applied to enhance environment-sensitive properties. Temperature-sensitive polymers demonstrate lower critical solution temperatures (LCST), which provide reversible high swelling at low temperatures and low swelling at high temperatures.[1–4] Similarly, pH-sensitive polymers synthesized with either acidic or basic components demonstrate reversible swelling/deswelling in an acidic or basic medium.[5–14]

Hoffman and Dong[7] combined these two properties by synthesizing cross-linked pH/temperature-sensitive hydrogels. Positively charged hydrogels were prepared by copolymerizing in varying ratios of *N*-isopropylacrylamide and *N*,*N*′-dimethylaminopropylmethacrylamide. Kim et al.[14] made beads formed from linear pH/temperature polymers, poly(*N*-isopropylacrylamide-co-butylmethacrylate-co-acrylic acid) and reported on the release of insulin through the polymeric system.

There have been several studies reported on the surface modification of porous membranes by grafting acrylic monomers utilizing corona discharge, glow discharge and UV techniques.[15–21] Iwata et al. reported on the graft polymerization of acrylamide onto a polyethylene[15,16] using corona discharge and of *N*-isopropylacrylamide onto a poly(vinylidene fluoride)[17] using the glow discharge technique. Osada et al.[18] grafted poly(methacrylic acid) onto a porous poly(vinyl alcohol) membrane using plasma treatment, and their ion transport, albumin and poly(ethylene glycol) permeation behaviours were studied. X-ray photoelectronspectroscopy (XPS) was utilized to confirm the graft reaction.[15–18] Recently, Ito et al.[19] reported on the water permeation through porous polycarbonate membrane having poly(carboxylic acid) on the membrane surface by pH and ionic strength.

It is our objective to review the intelligent pH/temperature-sensitive membrane by grafting acrylic acid (AAc) and *N*-isopropylacrylamide (NIPAAm)

onto the porous polymer membrane, which was prepared by the plasma or UV polymerization technique.

7.2 Experimental

7.2.1 Materials

Acrylic acid (AAc) was obtained from Junsei Chemical Co. and used as a grafting monomer. It was purified by using a glass column filled with an inhibitor remover (Aldrich Co., Milwaukee, WI) and stored in a dark and cold place. *N*-isopropylacrylamide (NIPAAm; Tokyo Kasei Chemical Co., Japan) was used after recrystallization in hexane and toluene (40 : 60 in vol %). Riboflavin was purchased from Junsei Chemical Co. and used without any further treatment. Porous polyamide membrane from Gelman Science Co. with 127 μm in thickness, 0.45 μm pores and 1,1-dimethyl-2-picrylhydrazyl (DPPH) (Aldrich Co.) was used for the determination of peroxides produced by UV irradiation.

7.2.2 Determination of peroxide produced by UV irradiation

The PSF membrane was irradiated by a medium-pressure mercury lamp (450 W, Ace Glass Inc.) at room temperature in air for a predetermined time. The membrane samples were prepared to an area of 8.675 cm^2 and irradiated at a distance of 5 cm below the UV lamp for all samples. Peroxides produced on the membrane surface were determined by DPPH. The DPPH (1×10^{-4} mol/l) solution in toluene was degassed by nitrogen blowing for 60 min. The UV-treated PSF membrane was quickly dipped into the DPPH solution at 60 °C for 2 hours in a shaking water bath. Using the reacted solutions, a consumed amount of DPPH due to peroxides produced on the surface was measured by a UV spectrophotometer (UV-2101PC, Shimadzu, Kyoto, Japan) at 520 nm. A calibration curve was obtained by using a DPPH solution of a known concentration.

7.2.3 Preparation of stimuli-responsive polymeric membranes

7.2.3.1 Preparation of poly(amide-g-NIPAAm) and poly(amide-g-(AAc-NIPAAm))

For the plasma polymerization, a bell jar type plasma reaction apparatus was used to accommodate the AAc and NIPAAm monomers. This low pressure glow discharge apparatus has a radio-frequency generator (13.56 MHz, 0–300 W

Table 7.1 Effect of feed composition on the graft yield of surface modified polyamide membranes using plasma polymerization method at 60 °C for 2 hours

Sample	Feed composition NIPPAm/AAc (w/w)	Concentration (wt %)	Graft yield (μg/cm²)
PA	—	20	—
PNA1	100:0	20	202
PNA2	95:5	20	222
PNA3	90:10	20	297
PNA4	85:15	20	197

power) and an impedance matching circuit. After washing and drying, the porous polyamide membrane was applied to 50 mtorr and 30 W argon plasma for 30 seconds. The sample was exposed immediately to the air and immersed in the monomer solution. The AAc and NIPAAm monomer solutions were prepared by dissolving each monomer in deionized water (see Table 7.1) for sample designation. To remove the oxygen remaining in the solution, nitrogen gas was bubbled into the solution at room temperature for 30 min. The graft polymerization of AAc and NIPAAm onto the plasma-treated polyamide was performed for 2 h at 60 °C.

The grafting amount of treated polyamide membranes was calculated as follows:

$$\text{Graft yield } (\mu g/cm^2) = \frac{(W_t - W_0)}{(A)} \times 100,$$

where W_0, W_t and A represent the weight of the membrane before and after the graft reaction and membrane area, respectively.

7.2.3.2 Preparation of PSF-g-AAc membrane

The PSF membrane (17.35 cm²) was weighed precisely and irradiated at the same conditions as in the peroxide-determination experiments. 20 wt. % AAc aqueous solution was degassed by nitrogen blowing for 60 min. UV-treated PSF was quickly dipped into the solution at 60 °C for 2 h in a shaking water bath. The grafted membranes were washed with deionized water at 70 °C for 24 h and dried in a vacuum oven at 40 °C for 48 h. Details on analytical equipment and methods and the solute permeation experiments can be found in the references.[20,21]

7.3 Results and discussion

7.3.1 Characterization of stimuli-responsive polymeric membranes

7.3.1.1 Poly(amide-g-NIPAAm) and poly(amide-g-(AAc-NIPAAm)) membranes

The surface of AAc and NIPAAm grafted polyamide membrane was analysed by *XPS*[22–25] as shown in Fig. 7.1 and 7.2. The PNA membrane surface showed new peaks resulting from the incorporation of –C–O– at ~ 286.6 eV and ester carbon atoms at ~ 289.1 eV (O=C–O–). The poly(amide-g-NIPAAm) (PNA1) surface showed a new peak ~ 288.0 eV as O=C–N, indicating the presence of *N*-isopropyl groups on the polyamide surface. The oxygen peak in the C=O groups appeared at 529 eV for membranes. The peak at high binding energy region (533.5 eV) is a peak for the oxygen in the –OH groups, indicating the presence of –COOH groups on the grafted PNA membrane surface. As the AAc content increases, the –OH peak becomes larger relative to the peak of the C=O bond.

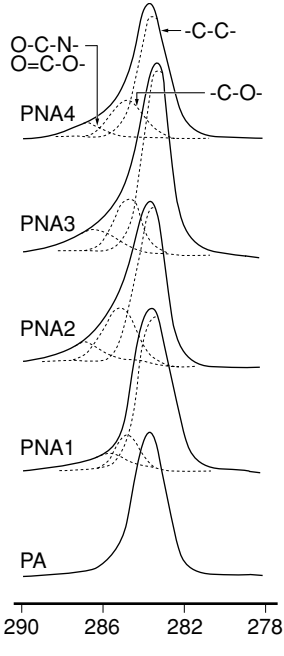

7.1 XPS carbon 1S core level spectra of polyamide and grafted polyamide surfaces.

In the present study, the graft yields of the polymer range between 197–297 μg/cm^2 (see Table 7.1) and increase with increasing AAc content, except for the PNA4 sample. When the AAc content was more than 10 wt % of the feed composition, the graft yield of the membrane decreased. These results also showed that upon increasing the pH, the reactivity ratio decreased and increased for acrylic acid and acrylamide, respectively. The pH of the feed solution in Table 7.1 decreased from 4.7 to 2.7 as acrylic acid increased. Therefore, the lower graft yield in PNA4 is probably due to the low reactivity of NIPAAm at above 10 wt % of acrylic acid in the feed composition because of the low pH.

7.3.1.2 PSF-g-AAc membranes

It is known that PSF and poly(ether sulfone) show strong absorption bands in the wavelength range between 250 and 300 nm.[26] During UV irradiation, chain scission, cross-linking and extensive yellowing occur. UV irradiation in a vacuum or in air yields several degraded products, such as gaseous products, oligomeric or polymeric sulfonic acids, and polymeric peroxides.

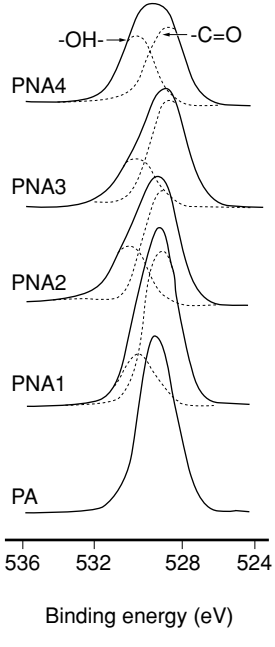

7.2 XPS carbon 1S core level spectra of polyanide and grafted polyamide surfaces.

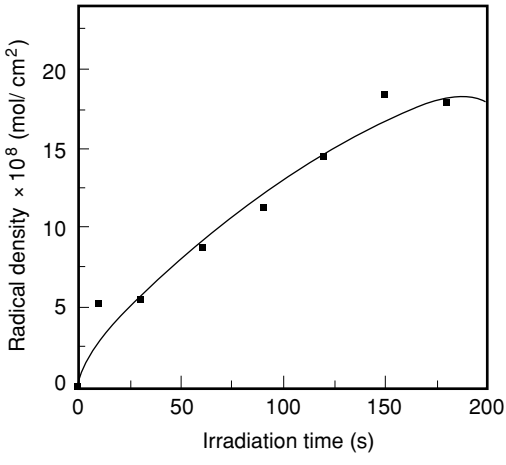

7.3 Effect of radical density as a function of UV irradiation time as determined by the DPPH method.

Kuroda et al.[26] reported the tendency of chain scission and cross-linking of poly(ether sulfone) films below and above the glass transition temperature (T_g). Chain scission and cross-linking occur simultaneously in all ranges of experimental temperatures. Cross-linking is dominant at above 170 °C, while chain scission is more important at room temperature. Yamashita et al.[27] reported on the photodegradation of poly(ether sulfone) and PSF in the presence and absence of oxygen over the temperature range from room temperature to 225 °C, and investigated the quantum yields for cross-linking and chain scission by gel permeation chromatography (GPC) measurements. They showed similar results on the temperature effect of chain scission and cross-linking from the degradation of poly(ether sulfone). However, in the case of PSF, chain scission occurs even at higher temperatures.

Figure 7.3 shows the radical density of a UV-irradiated PSF membrane with varying irradiation times. The radical density increased with increasing irradiation time up to 150 seconds, but decreased slightly with further irradiation. This indicates that the produced peroxides are partially converted into inactive species, which cannot generate radicals.

Table 7.2 summarizes the amount of PAAc grafted onto the surface of the PSF membrane. The graft amount of PAAc increased with irradiation time up to 150 s, exhibiting the same tendency as did the result from the radical density data. When we further irradiated the PSF samples, the graft amount and radical density of the modified PSF membrane decreased slightly. This means that long irradiation times do not always provide a merit in the amount of PAAc grafted onto the PSF membranes. Characterization and permeation experiments were done for grafted membranes irradiated up to 150 s.

Table 7.2 Effect of UV irradiation time on the amount of grafting of surface-modified PSF membranes

Sample[a]	Irradiation time (s)	Amount of grafting ($\mu g/cm^2$)
PSF	—	—
UA1	10	53
UA2	30	57
UA3	90	62
UA4	120	71
UA5	150	104
UA6	180	98

[a]A 20 wt% aqueous solution of AAc was used.

Table 7.3 XPS surface analysis of surface-modified PSF membranes by UV irradiation technique

	Atomic (%)			
Sample	C_{1S}	O_{1S}	S_{2P}	O_{1S}/S_{2P}
PSF	90.70	3.92	5.37	0.73
UA1	90.81	4.18	5.01	0.83
UA2	91.69	4.00	4.11	0.97
UA3	87.93	6.28	5.60	1.08
UA4	90.20	5.43	4.37	1.24
UA5	91.08	5.08	3.85	1.32

To investigate the chemical composition of the membrane surface, XPS analyses of the PSF and PSF-g-AAc membranes were performed and are summarized in Table 7.3. The atomic concentration of S_{2p} for the unmodified PSF membrane is 5.37% and can be used as a reference on the basis that it does not change after UV irradiation. The atomic concentration of grafted membranes, the ratio of O_{1S} to S_{2P}, gradually increases upon prolonging the UV irradiation time up to 150 s (UA5). This indicates that the atomic concentration of O_{1S} in the surface region increases as AAc is grafted further.

An inert gas ion beam was used to ablate the sample surface, and the chemical composition of the new surface was determined by XPS surface analysis. XPS ion-sputter depth profiling is a valuable means of determining the thickness of the graft layer. The effective thickness of the graft layer was calculated and the thickness of the PAAc grafted onto the PSF membrane surface in UA1 and UA3 was determined to be around 80–100 nm. Moreover, we can also determine the thickness of the graft layer from the relation

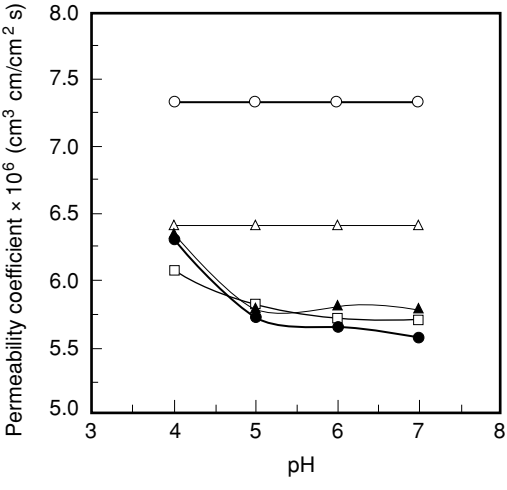

7.4 Effect of pH on the permeation of riboflavin through PA and PNA membranes measured at 37 °C. —○— PA, —△— PNA1, —□— PNA2, —●— PNA3, —▲— PNA4.

$l = m/\rho A$, where l is the thickness of the graft layer, m the amount of grafting, ρ the density of the graft PAAc and A the unit area. Here, the PAAc density is approximately 1. The thickness of the UA1 and UA3 samples can be calculated to be approximately 530–620 nm, indicating a large discrepancy between the thickness values determined by the two methods. The thickness determined by an XPS method is much smaller than that by the amount of grafting. This result suggests that PAAc was grafted not only onto the surface of the PSF membrane but also onto the inside of the PSF membrane. In this case, an aqueous AAc solution was expected to diffuse into the PSF membrane, and the vinyl monomer was grafted not only at the surface but also within the membrane. Tazuke[28] reported that acrylamide was grafted more from the bulk of the hydrophobic-oriented polypropylene membranes than on the surface of the membranes when the solvent had strong interactions with the base polymer.

7.3.2 Riboflavin permeation through stimuli-responsive membranes

7.3.2.1 Poly(amide-g-NIPAAm) and poly(amide-g-(AAc-NIPAAm)) membranes

The riboflavin release patterns of PA and PNA membranes at different pH regions and at 37 °C are demonstrated in Fig. 7.4. The permeation of riboflavin was also measured at various temperatures and at neutral pH, as shown in

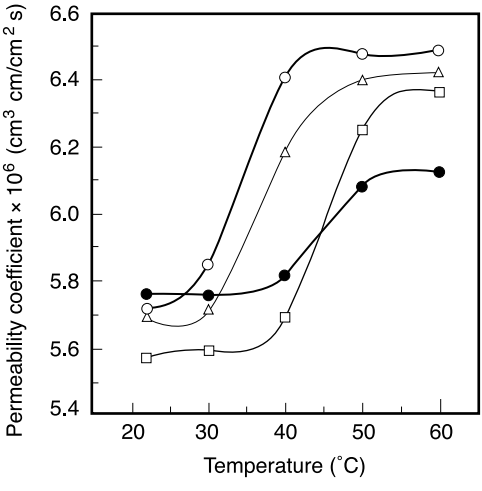

7.5 Effect of temperature on the permeation of riboflavin through PA and PNA membranes measured at pH 7. —○— PNA1, —△— PNA2, —□— PNA3, —●— PNA4.

Fig. 7.5. In PA and PNA1 membranes that did not have acrylic acid on the polyamide surface, the release profile of riboflavin was constant as pH varied. However, the PNA2, PNA3 and PNA4 membranes showed a pH-dependent release of riboflavin. The permeability of riboflavin decreased from 6.3×10^{-6} cm^3 cm/cm^2 s at pH 4 to around 5.7×10^{-6} cm^3 cm/cm^2 s at pH 7. The absolute permeability value was one order of magnitude higher than that of the PVDF membrane[29] in our previous study due to the larger pore radius of the PA membrane.

However, the magnitude of the decrease of permeability at pH 4 to pH 7 was somewhat lower than that of the PVDF membrane. This may be caused by two possible factors: the large pore size of the PA membrane and the lower acrylic acid content in the feed solution.

The effective graft chain for permeation is present on the inner pore or on the edge of the pore, and may shrink or enlarge upon pH changes. Large pore size may reduce the effectiveness of the pH-dependent permeation of small solutes unless the graft chain is long enough to cover the pores. Competitive AAc and NIPAAm reaction reduced the number of the AAc content in the chain and lowered the pH sensitivity, which is defined as the ratio of permeability at pH 4 and pH 7.

The effective pore size of the PNA membranes at any pH and temperature can be calculated using a simple Hagen–Poiseuille's law and the ratio of flux or permeability coefficient of the virgin and graft membrane.

Table 7.4 Determination of effective pore radii and effective areas for permeation at pH 4 and 7 through pH-sensitive polyamide membranes estimated by Eq. (7.1)

Sample	pH 4		pH 7		$\frac{A_{pH\,4}}{A_{pH\,7}}$(%)
	r(Å)	A^* ($\times 10^6$ Å^2)	r(Å)	A^* ($\times 10^6$ Å^2)	
PA	2250	15.90	2250	15.90	100.0
PNA1	2176	14.88	2176	14.88	100.0
PNA2	2147	14.48	2115	14.05	103.1
PNA3	2167	13.75	2103	13.89	106.2
PNA4	2172	14.82	2121	14.13	104.9

*A = Effective membrane area for permeation of solute.

$$r_0/r_1 = [J_0/J_i]^{\frac{1}{4}} \qquad [7.1]$$

Here, J_0 and J_i are the fluxes of solute through the PA and PNA membranes respectively, at 37 °C in varying pH ranges.

The effective pore radius was reduced from 2250 Å to 2103 Å upon grafting and expansion of the graft chain at pH 7 (Table 7.4). The above results show the possibility of controlling the pH region, in which the riboflavin permeability changes most sensitively with pH, by choosing the nature of the polymers to be grafted.

As NIPAAm is grafted on the porous polyamide membrane using the plasma grafting technique, the permeability changes with temperature. Poly(NIPAAm)[1,2] is known to have LCST at around 31–33 °C. Below LCST, poly(NIPAAm) forms hydrogen bonds with water and exists in solution form. However, above LCST, inter- and intramolecular interaction in poly(NIPAAm) is much stronger, resulting in an undissolved state. In this state, the hydrogen bonding between grafted poly(NIPAAm) (PNA1) and water breaks down and the mobility of the polymer chain, inter- and intramolecular interactions, and the hydrophobic interaction due to the presence of the alkyl groups in the polymer chain increase.[30] The grafted poly(NIPAAm) chain shrinks, leading to an enlargement of the effective pore size in the porous polyamide membrane. Using the same Hagen–Poiseuille's equation and Eq. (7.1), the effective pore radius was calculated to be 2113 Å at 30 °C and the graft chains shrink to 2175 Å at 50 °C for PNA2 membrane, resulting in an expansion of the effective area for permeation, as indicated in increase in $A_{50\,°C}/A_{30\,°C}$ in Table 7.5.

PNA2, PNA3 and PNA4 used the acrylic acid as a comonomer with NIPAAm. In this case, the transition temperatures of riboflavin permeation change from 35 °C to 50 °C, as illustrated in Fig. 7.5.

Table 7.5 Determination of effective pore radii and effective areas for permeation at 30 °C and 50 °C through temperature-sensitive polyamide membranes estimated by Eq. (7.1)

Sample	Temperature 30 °C		Temperature 50 °C		$\frac{A_{50\,^{\circ}C}}{A_{30\,^{\circ}C}}$ (%)
	r(Å)	A^* ($\times 10^6$ Å^2)	r(Å)	A^* ($\times 10^6$ Å^2)	
PA	2250	15.90	2250	15.90	100.0
PNA1	2126	14.20	2182	14.96	100.3
PNA2	2113	14.03	2175	14.86	105.9
PNA3	2102	13.88	2162	14.69	105.9
PNA4	2118	14.09	2147	14.48	102.8

*A = Effective membrane area for permeation of solute.

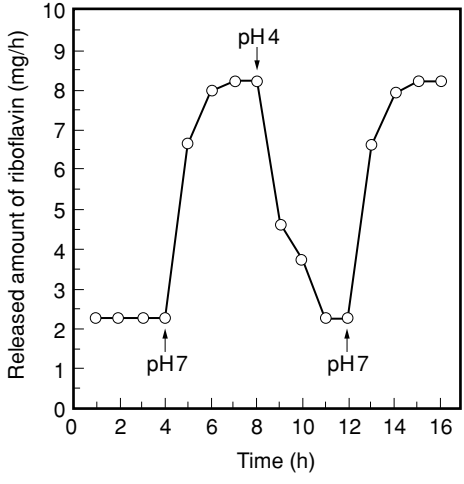

7.6 Reversible release pattern of riboflavin from PNA3 membrane with step-wise changing of the pH between 7 and 4 measured at 37 °C. —○— PNA3.

In order to study the pH/temperature-dependent change of the permeability of riboflavin, the permeation of riboflavin through the PNA3 membrane was investigated by alternating pH from 7 to 4 (Fig. 7.6), and temperature from 30 to 50 °C (Fig. 7.7). It was observed that a discontinuous change in concentration of riboflavin was brought about by stepwise changing of the temperature or pH. When the permeation experiment of riboflavin through the PNA3 membrane was conducted by changing pH or temperature, the riboflavin release increased rapidly but reverted to the same permeability within an hour.

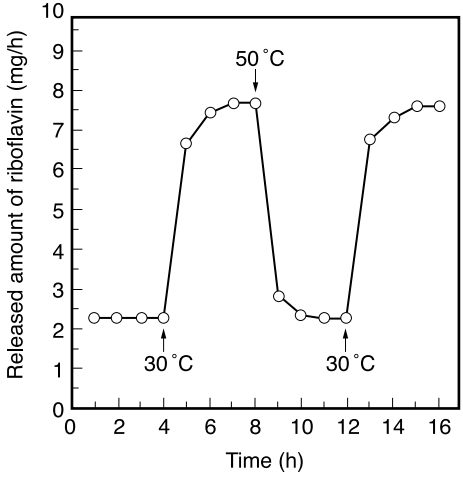

7.7 Reversible concentration control of riboflavin from PNA3 membrane with step-wise changing of the temperature between 30 °C and 50 °C measured at pH 7. —○— PNA3.

7.3.2.2 PSF-g-AAc membranes

Riboflavin permeability through the original PSF membrane and the PSF-g-AAc membranes is shown in Fig. 7.8, measured at different pH values. Note that the virgin PSF membrane exhibits no response to the change in pH, whereas PSF-g-AAc membranes are responsive to the pH change. A remarkable decline in permeability is noted in the range of pH 4–5. From these data, it is clear that the grafted PAAc is responsible for the permeability decline in riboflavin permeation.

It has been reported that the pK_a value of poly(acrylic acid) (PAAc) is 4.8.[20,30] Above pH 4.8, the carboxylic acid groups of the grafted PAAc chains are dissociated into carboxylate ions and have an extended conformation because of the electrostatic repulsion forces between the chains. Extended chains block the pores of the PSF membrane, causing a decrease in the permeability. At below pH 4.8, carboxylic acid groups do not dissociate: the grafted PAAc chains will shrink and be precipitated on the surface. Thus, the pores become open and permeability increases sharply. These conformational changes are obviously due to both intra- and intermolecular interactions between the grafted PAAc chains.

As the amount of grafted PAAc increases further, pore blocking overwhelms the conformational changes of the grafted chains due to the interactions of the polymer chains, causing only small changes in the permeability of riboflavin in response to the pH. Therefore, for a UA5 sample, the extension and

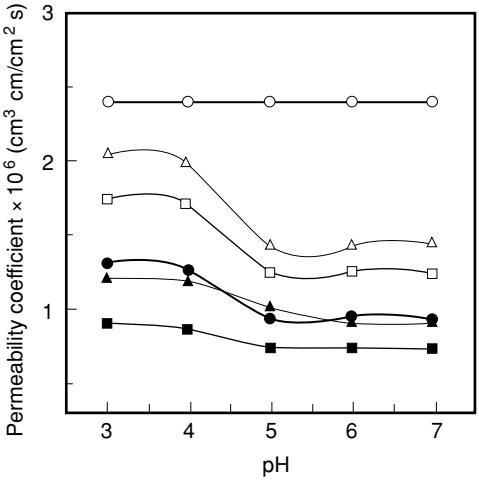

7.8 Effect of pH on the riboflavin permeation through (*a*) PSF (○), (*b*) UA1 (△), (*c*) UA2 (□), (*d*) UA3 (●), (*e*) UA4 (▲), (*f*) UA5 (■) membranes.

shrinkage of the grafted chains are hindered, and the extent of the change in the permeability is reduced, meaning that the permeability depends on the amount of grafting and the environmental pH.

7.4 Conclusions

We have prepared pH/temperature-sensitive polymer membranes by grafting AAc or NIPAAm or AAc and NIPAAm on the surface of polyamide and polysulfone membranes, utilizing plasma and UV radiation techniques. The structure of the graft chain was confirmed by XPS and ATR-FTIR spectra. Through this study, we investigated the morphology and permeability of the riboflavin of the unmodified and modified polymer membranes. AAc or NIPAAm or AAc and NIPAAm-grafted polymer membranes showed the pH or temperature and pH-dependent permeation behaviours of riboflavin, respectively.

Therefore, the present stimuli-responsive membrane system was valid in pH/temperature-responsive drug delivery or intelligent separation membranes. This study envisioned the possibility of controlling the permeability of the membrane by varying the pH of the external solution. These pH/temperature-responsive membranes will be useful for sensing and modulating external chemical signals, and also for drug-delivery applications, because they change their chain conformation according to the surrounding circumstances.

Acknowledgement

Financial support from the Korea Institute of Science & Technology Evaluation and Planning through National Research Laboratory Programme is greatly appreciated.

References

1 Okano T, Bae Y H, Jacobs H and Kim S W, 'Thermally on–off switching polymers for drug permeation and release' *J. Controlled Release*, 1990, **11**, 255.
2 Okano T, Bae Y H and Kim S W, 'On–off thermocontrol of solute transport: II. Solute release from thermosensitive hydrogels' *Pharmaceut. Res.*, 1991, **8**, 624.
3 Nozawa I, Suzuki Y, Sato S, Sugibayashi K and Morimoto Y, 'Preparation of thermo-responsive polymer membranes', *J. Biomed. Mater. Res.*, 1991, **25**, 243.
4 Okahata Y, Lim H J, Nakamura G and Hachiya S, 'A large nylon capsule coated with a synthetic bilayer membrane permeability control of NaCl by phase transition of the dialkylammonium bilayer coating', *J. Amer. Chem. Soc.*, 1983, **105**, 4855.
5 Kitano H, Akatsuka Y and Ise N, 'pH-responsive liposomes which contain amphiphiles prepared by using lipophilic radical initiator', *Macromolecules*, 1991, **24**, 42.
6 Siegel R A, Falamarzian M, Firestone B A and Moxley B C, 'pH-controlled release from hydrophobic/polyelectrolyte copolymer hydrogels', *J. Controlled Release*, 1988, **8**, 179.
7 Hoffman S and Dong L, 'A novel approach for preparation of pH-sensitive hydrogels for enteric drug delivery', *J. Controlled Release*, 1991, **15**, 141.
8 Park T G and Hoffman A S, 'Synthesis and characterization of pH- and/or temperature-sensitive hydrogels', *J. Appl. Polym. Sci.*, 1992, **46**, 659.
9 Iwata H and Matsuda T G, 'Preparation and properties of novel environment-sensitive membranes prepared by graft polymerization onto a porous membrane', *J. Membrane Sci.*, 1988, **38**, 185.
10 Klumb L A and Horbett T A, 'Design of insulin delivery devices based on glucose sensitive membranes', *J. Controlled Release*, 1992, **18**, 59.
11 Kim J H, Kim J Y, Lee Y M and Kim K Y, 'Controlled release of riboflavin and insulin through crosslinked poly(vinyl alcohol)/chitosan blend membrane', *J. Appl. Polym. Sci.*, 1992, **44**, 1823.
12 Chung J, Ito Y and Imanishi Y, 'An insulin-releasing membrane system on the basis of oxidation reaction of glucose', *J. Controlled Release*, 1992, **18**, 45.
13 Ito Y, Kotera S, Ibana M, Kono K and Imanishi Y, 'Control of pore size of polycarbonate membrane with straight pores by poly(acrylic acid)', *Polymer*, 1990, **31**, 2157.
14 Kim Y H, Bae Y H and Kim S W, 'pH/temperature-sensitive polymers for macromolecular drug loading and release', *J. Controlled Release*, 1994, **28**, 143.
15 Iwata H, Kishida A, Suzuki M, Hata Y and Ikada Y, 'Oxidation of polyethylene surface by corona discharge and the subsequent graft polymerization', *J. Polym. Sci. Polym. Chem.*, 1988, **26**, 3309.

16 Suzuki M, Kishida A, Iwata H and Ikada Y, 'Graft copolymerization of acrylamide onto a polyethylene surface prepared with a glow discharge', *Macromolecules*, 1986, **19**, 1804.
17 Iwata H, Oodate M, Uyama Y, Amemiya H and Ikada Y, 'Preparation of temperature-sensitive membranes by graft polymerization onto a porous membrane', *J. Membrane Sci.*, 1991, **55**, 119.
18 Osada Y, Honda K and Ohta M, 'Control of water permeability by mechanochemical contraction of poly(methacrylic acid)-grafted membranes', *J. Membrane Sci.*, 1986, **27**, 327.
19 Ito Y, Inaba M, Chung D J and Imanishi I, 'Control of water permeation by pH and ionic strength through a porous membrane having poly(carboxylic acid) surface-grafted', *Macromolecules*, 1992, **25**, 7313.
20 Kim J H, Lee Y M and Chung C N, 'Permeation of drug through porous polyurethane membranes grafted with poly(acrylic acid)', *J. Korean Ind. Eng. Chem.*, 1992, **3**, 233.
21 Lee Y M, Ihm S Y, Shim J K, Kim J H, Cho C S and Sung Y K, 'Preparation of surface-modified stimuli-responsive polymeric membranes by plasma and ultraviolet grafting methods and their riboflavin permeation', *Polymer*, 1994, **36**, 81.
22 Palit S R and Ghosh P, 'Quantitative determination of carboxyl endgroups in vinyl polymers by the dye-interaction method, a theoretical investigation of molecular core binding and relaxation', *J. Polym. Sci.*, 1962, **58**, 1225.
23 Beamson G and Briggs D, *High Resolution XPS of Organic Polymers*, Wiley, UK, 1992, pp. 110–11, 188–201.
24 Clark D T, Cromarty B J and Dilks A H R, 'A theoretical investigation of molecular core building and relaxation energies in a series of oxygen-containing organic molecules of interest in the study of surface oxidation of polymer', *J. Polym. Sci. Polym. Chem.*, 1978, **16**, 3173.
25 Rabek J F, *Polymer Degradation*, 1st. edn., Chapman & Hall, London, 1995, p. 317.
26 Kuroda S I, Mita I, Obata K and Tanaka S, 'The tendency of chain scission and crosslinking of poly(ether sulfone) films below and above the glass transition temperature (Tg)', *Polym. Degrad. Stabil.*, 1990, **27**, 257.
27 Yamashita T H, Tomitaka T, Kudo K, Horie K and Mita I, 'The photodegradation of poly(ether sulfone) and PSF in the presence and absence of oxygen', *Polym. Degrad. Stabil.*, 1993, **9**, 47.
28 Tazuke S, Matoba T, Kimura H and Okada T, ACS Symposium Series 121, American Chemical Society, Washington, DC, 1980, p. 217.
29 Lee Y M and Shim J K, 'Plasma surface graft of acrylic acid onto porous poly(vinylidene fluoride) membrane and its riboflavin permeation', *J. Appl. Polym. Sci.*, 1996, **61**, 1245.
30 Mandel M, 'Energies in a series of oxygen-containing organic molecules of interest in the study of surface oxidation of polymers', *Eur. Polym. J.*, 1970, **6**, 807.

8

Mechanical properties of fibre Bragg gratings

XIAOGENG TIAN AND XIAOMING TAO

8.1 Introduction

Self-organized Bragg grating in optical fibres, or changes in refractive index induced by radiation was first observed[1,2] in 1978. Since permanent Bragg gratings were first written by Meltz et al.[3] in 1989 by the transverse holographic method, they have attracted great attention in the fields of telecommunication, sensing, smart materials and structures. Fibre Bragg grating (FBG)-based sensors have some distinct advantages. First, they give an absolute measurement insensitive to any fluctuation in the irradiance of the illuminating source, as the information is directly obtained by detecting the wavelength-shift induced by strain or temperature change. Secondly, they can be written into a fibre without changing the fibre size, making them suitable for a wide range of situations where small diameter probes are essential, such as in advanced composite materials, the human body, etc. Thirdly, they can be mass produced with good repeatability, making them potentially competitive with traditional strain gauges from the fabrication cost point of view.[4,5] Finally, they can be multiplexed in a way similar to methods used on conventional fibre-optic sensors, such as wavelength-, frequency-, time- and spatial-division-multiplexing and their combination,[6,7] making quasi-distributed sensing feasible in practice.

Because of these advantages, FBGs have been applied as embedded sensors to monitor or measure the internal strain of composite structures.[8–13] Friebele et al.[9,10] reported internal distribution strain sensing with fibre grating arrays embedded in continuous resin transfer moulding™ (CRTM™) composites. Bullock and his colleagues[11] used a translaminar embedded fibre grating sensor system to monitor the structure of composites. Du et al.[14] embedded fibre Bragg gratings in a glass woven fabric laminated composite beam for internal strain measurements. FBGs are also used in mine operating accurate stability control[15] and medical monitoring.[16]

With FBG sensors being prepared for field applications, growing interest is focused on the mechanical reliability of the fibre gratings. The influence of various parameters like humidity,[17,18] chemical composition of coating,[19]

chemical agent,[20] stripping methods[21,22] and fibre splicing[23] have been investigated. At the same time, more than ten different models have been developed to estimate the lifetime from static and dynamic fatigue measurement under different environmental conditions.[24–26] In this chapter, we will examine the influence of the fabrication procedure and the mechanical properties of fibre Bragg grating sensors.

8.2 Fabrication techniques

8.2.1 Optical fibres

As shown in Fig. 8.1, an optical fibre consists of a core surrounded by a cladding whose refractive index is slightly smaller than that of the core. The optical fibre is coated during the fibre drawing process with a protective layer. Inside the fibre core, light rays incident on the core-cladding boundary at angles greater than the critical angle undergo total internal reflection and are guided through the core without refraction. Silica glass is the most common material for optical fibres, where the cladding is normally made from pure fused silica, and the core from doped silica containing a few mol % of germania. Other dopants, such as phosphorus, can also be used. Extra-low absorption occurs in a germanosilicate fibre, with a local minimum attenuation coefficient $\alpha = 0.3$ dB/km at 1.3 μm and an absolute minimum $\alpha = 0.16$ dB/km at 1.55 μm. Therefore, light in the two windows travels down tens of kilometres of fibre without strong attenuation in a correctly guided mode condition.

8.2.2 Fibre Bragg gratings

A fibre Bragg grating consists of a modulation in the refractive index, $n(z)$, along a short length (z) of the core in germania-doped silica fibre with a period of Λ, which is given by:

$$n(z) = n_0 + \Delta n_0 \cdot \cos[(2\pi/\Lambda) \cdot z + \phi_0] \qquad [8.1]$$

where n_0 is the linear refractive index for a guided mode in the fibre core, Δn_0 is

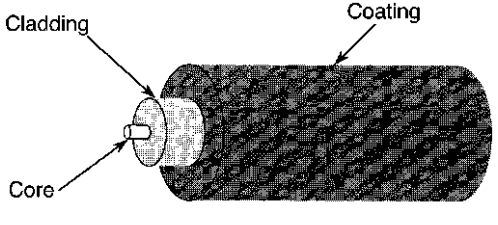

8.1 Structure of optical fibre.

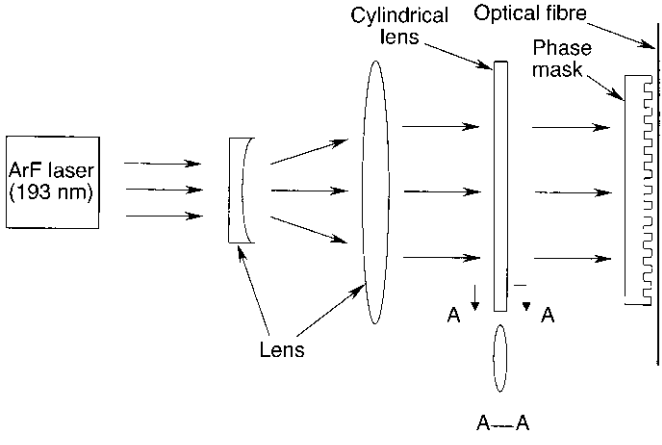

8.2 The set-up of FBG fabrication.

the modulation amplitude of the refractive index and ϕ_0 is the initial phase of the grating.

The inscription of permanent Bragg grating can be achieved in the core of an optical fibre by interference of two coherent ultra-violet light beams.[3] The grating thus has a holographically induced refractive index modulation with a period $\Lambda = \lambda_{uv}/2\sin(\theta/2)$, where θ is the angle between the two writing beams of wavelength λ_{UV}. When a broadband light source is coupled into the fibre, those components with wavelengths that satisfy the Bragg condition are strongly reflected, but all other components pass through the grating with negligible insertion loss and no change in signal. The central reflecting wavelength, referred to as the Bragg wavelength (λ_B) of a fibre grating, is determined by the Bragg condition:

$$\lambda_B = 2n_0\Lambda \qquad [8.2]$$

The central reflectivity is given by:

$$R = \tanh^2(\pi\Delta n_0 L/\lambda_B) \qquad [8.3]$$

where L is the grating length. The modulation amplitude of the refractive index, Δn_0, represents the grating strength and is dependent on the time of exposure to UV illumination. The width of the FBG reflecting band is determined by L and Δn_0. The higher the values of Δn_0 and L, the narrower the bandwidth.

Nowadays, the gratings are often fabricated by phase mask technology. Figure 8.2 shows an experimental set-up for writing Bragg gratings on single

mode germanium-doped silica fibres. The light is spread by using a lens after it is guided from an ArF excimer laser, then paralleled by passing through a cylindrical lens and focused on the optical fibre by using another cylindrical lens, which is normal to the other lens.

8.3 Mechanisms of FBG sensor fabrication

Why can UV irradiation cause a change in the refractive index? To date, there appear to be three possible mechanisms by which a photo-induced refractive index change can occur in germanosilica optical fibres: (i) through the formation of colour centres (GeE′), (ii) through densification and increase in tension, and (iii) through formation of GeH. Broadly speaking, all three mechanisms prevail in germanosilica optical fibres. The relative importance of each contribution depends on the type of optical fibre and the photosensitization process used.

8.3.1 The formation of colour centres (GeE′) and GeH

There are a lot of defects in the germanium-doped core. The paramagnetic Ge(n) defects, where n refers to the number of next-nearest-neighbour Ge atoms surrounding a germanium ion with an associate unsatisfied single electron, were first identified by Friebele et al.[27] These defects are shown schematically in Fig. 8.3.

The Ge(1) and Ge(2) have been identified as trapped-electron centres.[28] The characteristic absorption of Ge(1) and Ge(2) are 280 nm and 213 nm. The GeE′, previously known as the Ge(0) and Ge(3) centres, which is common in oxygen-deficient germania, is a hole trapped next to a germanium at an oxygen vacancy,[29] and has been shown to be independent of the number of next-neighbour Ge sites. Here, an oxygen atom is missing from the tetrahedron, while the germanium atom has an extra electron as a dangling bond. Other defects include the non-bridging oxygen hole centre (NBOHC), which is claimed to have absorption at 260 nm and 600 nm, and the peroxy radical, believed to have absorption at 163 nm and 325 nm.[30] Both are shown in Fig. 8.3.

If the optical fibre is treated with high temperature hydrogen, germania will decrease and the concentration of GeO molecules will be enhanced. The reduction process may occur as follows:

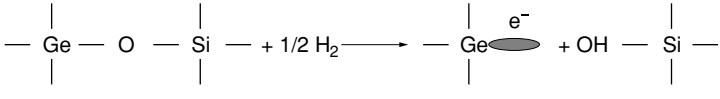

Most fibres, if not all, show an increase in the population of the GeE′ centre (trapped hole with an oxygen vacancy) after UV exposure. This is formed by

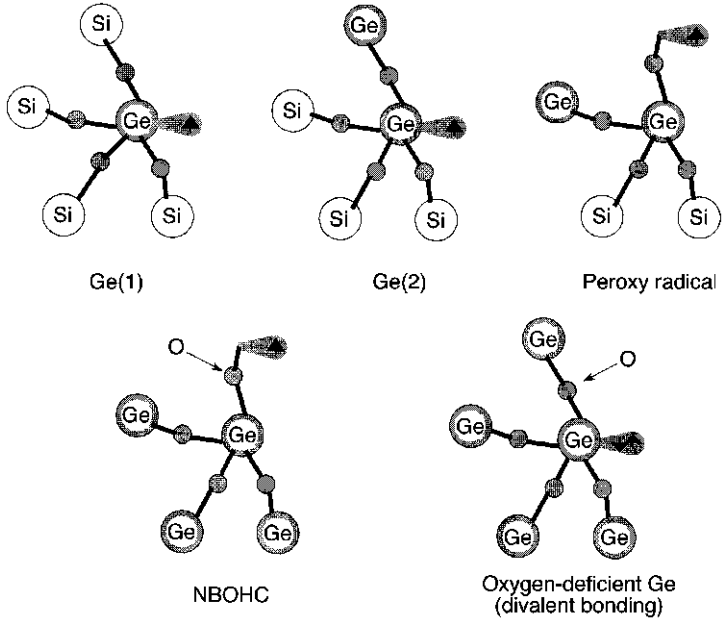

8.3 A schematic of proposed Ge defects of germania-doped silica.

the conversion of the electron-trapped Ge(I) centre, which absorbs at ~ 5 eV, and the GeO defect. GeO defect is shown in Fig. 8.4. It has a germanium atom coordinated with another Si or Ge atom. This bond has the characteristic 240 nm absorption peak that is observed in many germanium-doped photosensitive optical fibres.[31] On UV illumination, the bond readily breaks, creating the GeE′ centre. It is thought that the electron from the GeE′ centre is liberated and is free to move within the glass matrix via hopping or tunnelling, or by two-photon excitation into a conduction band. The change in the population of the GeE′ centres causes changes in the UV absorption spectra, which lead to a change in the refractive index of the fibre at a wavelength λ directly through the Kramers–Kronig relationship:[32]

$$\Delta n = \frac{1}{(2\pi)^2} \sum_i \int_{\lambda_1}^{\lambda_2} \frac{\Delta\alpha_i(\lambda') \cdot \lambda^2}{(\lambda^2 - \lambda'^2)} \mathrm{d}\lambda' \qquad [8.4]$$

where the summation is over discrete wavelength intervals around each of the i changes in measured absorption, $\Delta\alpha_i$. Therefore, a source of photoinduced change in the absorption at $\lambda_1 \leq \lambda' \leq \lambda_2$ will change the refractive index at wavelength λ. This process is common to all fibres. The colour centre model, originally proposed by Hand and Russel,[33] only explains part of the observed refractive index changes of $\sim 2 \times 10^{-4}$ in non-hydrogenated optical fibres.[34]

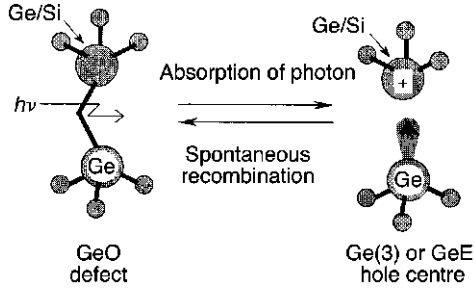

8.4 The capital GeO defect of germania-doped silica, in which the atom adjacent to germanium is either a silica or another germanium.

For molecular hydrogen, the suggested reaction is the formation of GeH and OH ions from a Ge(2) defect. The possible route may be as follows:

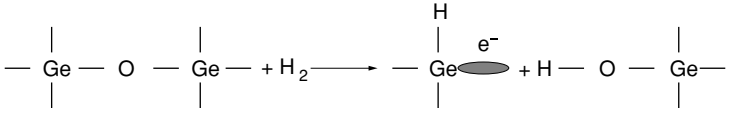

After the treatment, the concentration of GeE′ and GeH will increase greatly.

8.3.2 Densification and increase in tension

The refractive index of glass depends on the density of the material also,[35,36] so that a change in the volume through thermally induced relaxation of the glass will lead to a change Δn. The refractive index n is shown as:

$$\frac{\Delta n}{n} \approx \frac{\Delta V}{V} \approx \frac{3n}{2}\varepsilon \qquad [8.5]$$

where the volumetric change ΔV as a fraction of the original volume V is proportional to the fractional change ε in linear dimension of the glass.

A possible effect of the irradiation is a collapse of a higher-order ring structure leading to densification.[37] The densification of silica under UV irradiation is well documented.[38] The process of densification has been shown to occur in fibres, as evidenced by scans using an atomic force microscope of the surface of D-shape fibres and in etched fibres,[39] and in preform samples that were drawn into a D-shaped fibre.[35] These observations are on the surface of the sample and are unable to replicate the stress profiles within the core of the fibre directly. Direct optical measurement of in-fibre stress has indicated that, rather than the relief of the stress, tensile stress actually increases with an associated reduction in the average refractive index by $\sim 30\%$ of the observed UV induced refractive index change in non-hydrogen loaded, high germania-

content fibre. The changes in the stress profile of the fibre are consistent with the shift in the Bragg wavelength of a grating during inscription.[40]

8.4 Mechanical properties

8.4.1 Strength

Telecommunication optical fibres are made from silica glass with ring structures of Si–O tetrahedral. Defects or small imperfections which have been created on the surface of optical fibre during the fibre fabrication processing lead to a reduced fibre strength. Griffith suggested that these defects, called flaws, act as stress intensifiers and cause fracture, when they induce large enough stress to break chemical bonds mechanically.[41] The stress intensity factor K_I at a crack tip as a function of time, t, can be written as:[24]

$$K_I(t) = Y\sigma_\alpha(t)\sqrt{\alpha(t)} \qquad [8.6]$$

where Y is the dimensionless crack geometry shape parameter which is assumed to be constant for a given flaw type, σ_α is the applied stress and α is the flaw depth, i.e. the flaw size normal to the direction of the applied stress.

When the applied stress, σ_α, increases to its allowable maximum given by the intrinsic strength, S, of the crack, a catastrophic failure occurs. Equation (8.6) becomes:

$$K_{IC} = YS\sqrt{\alpha} \qquad [8.7]$$

K_{IC} is an intrinsic constant of silica and has been empirically determined to be: $K_{IC} = 0.79\ \text{MPa m}^{1/2}$.

If $n(\sigma)$ denotes a flaw distribution, then the number of the flaws which will fail between σ and $\sigma + \mathrm{d}\sigma$ is $n(\sigma)\mathrm{d}\sigma$. The total number of flaws whose strengths are less than σ is:

$$N(\sigma) = \int_0^\sigma n(\sigma)\mathrm{d}\sigma \qquad [8.8]$$

According to the Weibull distribution, the empirical form of the cumulative flaw distribution is given by:

$$N(\sigma) = \left(\frac{\sigma}{\sigma_0}\right)^m \qquad [8.9]$$

where σ is the applied stress to the fibre during the fatigue test, m is the scaling factor and σ_0 is a constant characteristic of the material. The probability of a breakage between stress level σ and $\sigma + \mathrm{d}\sigma$ is given by the joint probability that the sample contains a flaw whose strength falls into this interval and that the sample has survived a stress level σ:

$$dF(\sigma) = F(\sigma + d\sigma) - F(\sigma) = (1 - F(\sigma))n(\sigma)d\sigma \quad [8.10]$$

$F(\sigma)$, commonly referred to as the cumulative failure probability, is defined as the probability of breakage below a stress level σ. Consequently $1 - F(\sigma)$ is the survival probability. Assuming a group of M samples, $F(\sigma)$ is calculated as below:

$$F(\sigma) = \frac{i - 0.5}{M} \qquad i = 1, 2, \ldots, M \quad [8.11]$$

The failure stresses are listed with increasing magnitude as $\sigma_1, \sigma_2, \ldots, \sigma_i, \ldots, \sigma_M$ so that the cumulative failure probability $F(\sigma_i)$ can be determined. In the Weibull plot, the breaking stress σ is plotted versus the cumulative failure probability F. To compare different Weibull distributions, we use the median breaking stress, σ_m, which corresponds to 50% failure probability. Combining Eqs. (8.9) and (8.10) we obtain:

$$\log\left(\ln\frac{1}{1 - F(\sigma)}\right) = m\log\left(\frac{\sigma}{\sigma_0}\right) \quad [8.12]$$

The slope of the curve is the Weibull scaling parameter m, which indicates the shape of the distribution. Low m-values indicate a large range of surface flaw sizes, while high m-values indicate high surface quality and a close approach to the tensile strength of a flaw-free fibre under normal condition.[42] m-Values for pristine fibres are normally of the order of 80–150.

8.4.2 Young's modulus and hardness

The tensile test can provide information on the average Young's modulus and mechanical strength. A nano-indenter can measure the Young's modulus and hardness locally on a much smaller scale. Interest in load and displacement-sensing indentation testing as an experimental tool for measuring elastic modulus began in the early 1970s.[43] The nano-indenter is made of very hard material. When it is pressed on the surface of the tested material, deformation occurs on both the indenter and the tested material; according to the deformation of the material and the acted force, the material properties, such as Young's modulus and hardness, can be obtained.

The effects of the non-rigid indenter on the load-displacement behaviour can be effectively accounted for by defining a reduced modulus, E_r, through the equation:

$$\frac{1}{E_r} = \frac{1 - v_s^2}{E_s} + \frac{1 - v_i^2}{E_i} \quad [8.13]$$

where E_i and v_i are the Young's modulus and Poisson's ratio for the indenter and E_s and v_s are those of the material being tested. Therefore, the Poisson's

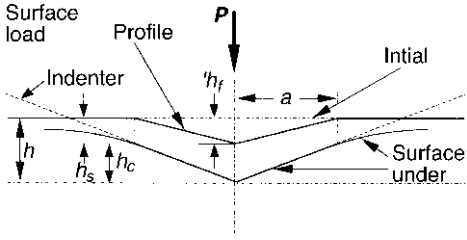

8.5 A schematic representation of load vs. indenter displacement showing quantities used in the analysis as well as the graphical interpretation of the contact depth.

ratio must be estimated for the material being tested to determine the modulus.

Using instrumented microhardness testing machines, the indentation load-displacement curve can be obtained as shown in Fig. 8.5. They are analysed according to the equation:

$$S = \frac{dP}{dh} = \frac{2}{\pi} E_r \sqrt{A} \qquad [8.14]$$

Here, $S = dP/dh$ is the experimentally measured stiffness of the upper portion of the unloading data, E_r is the reduced modulus (previously defined) and A is the projected area of the elastic contact.

The contact area at peak load can be determined by the geometry of the indenter and the depth of contact, h_c, assuming that the indenter geometry can be described by an area function $G(h)$ which relates the cross-sectional area of the indenter to the distance from its tip, h. Given that the indenter does not itself deform significantly, the projected contact area at peak load can then be computed from the relation $A = G(h_c)$. The functional form of G must be established experimentally prior to analysis.[43]

At any time during loading, the displacement, h, can be written as:

$$h = h_c + h_s \qquad [8.15]$$

where h_s is the displacement of the surface at the perimeter of the contact, which can be ascertained from the load-displacement data. At the peak, the load and displacement are P_{max} and h_{max}, respectively. We have $h_s = \varepsilon \frac{P_{max}}{S}$, ε is the geometrical constant, which relates to the geometry of the indenter.[44] ε for different geometries of indenter are listed in Table 8.1. The contact depth, h_c, can be expressed as:

$$h_c = h_{max} - \varepsilon \frac{P_{max}}{S} \qquad [8.16]$$

Table 8.1 ε for different shapes of indenter

Indenter	Conical indenter	Triangular pyramid	Flat punch
ε	0.72	0.75	1.00

So the contact area, A, can be obtained from Eq. (8.14) and combining it with Eq. (8.13), Young's modulus of the tested material can be expressed as:

$$E_s = \left[\frac{2}{\sqrt{\pi}}\frac{\sqrt{A}}{S} - \frac{1-v_i^2}{E_i}\right]^{-1} \cdot (1-v_s^2) \qquad [8.17]$$

The data obtained using the current method can be used to determine the hardness, H. The hardness is defined as the mean pressure the material will support under load. The hardness is computed from:

$$H = \frac{P_{\max}}{A} \qquad [8.18]$$

8.5 Influence of the UV-irradiation on mechanical properties

8.5.1 The influence on the mechanical strength

8.5.1.1 The mechanical strength of gratings not affected

Although type I grating has a reflectivity of only a few per cent, it can easily be written at any arbitrary position along the fibre.[45] Such FBG arrays are ideally suited for distributed sensing, where low reflectivity is not a major drawback. Askins et al.[46] and Hagemann et al.[47] have studied the mechanical strength of optical fibre containing FBG fabricated in this method. In their experiment, laser exposures occurred only immediately before the protective jacketing was applied during fibre drawing.

FBG sensors produced on-line during the process using an excimer laser pulse suffer no measurable loss of strength relative to unirradiated fibre. This emphasizes the fact that it is favourable to use draw-tower FBGs as sensor elements to overcome the problem related to fibre stripping and high fluence UV irradiation.

8.5.1.2 Mechanical strength degradation of gratings

Feced et al.[48] has studied the influence of different wavelength UV irradiation on the strength of optical fibres with a single pulse radiation. The single mode

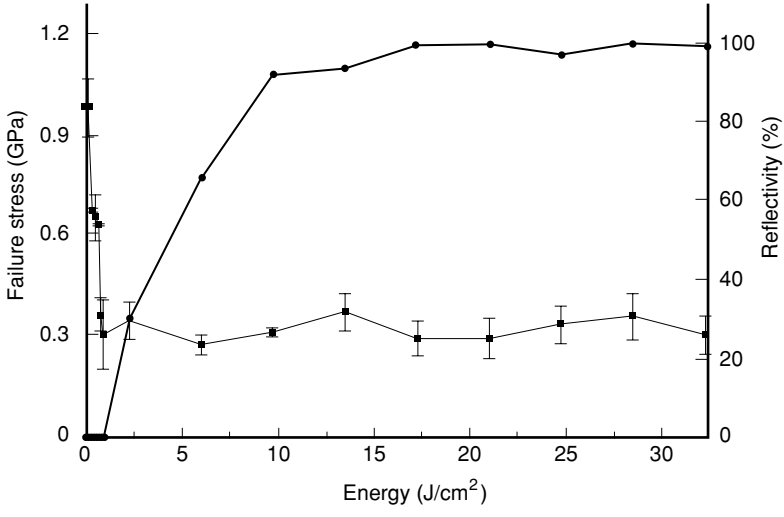

8.6 Mechanical strength and reflectivity: —■— strength, —●— reflectivity.

optical fibres used in their investigations were Corning's SMF-28 (~ 3 mol % of germanium), and a highly photosensitive germanium and boron (Ge–B) co-doped fibre (10 mol % of germanium) from the University of Southampton. Their results suggest that the fabrication of Bragg gratings using 193 nm irradiation will yield higher-strength gratings with enhanced reliability. A similar analysis shows that the difference in strength between Ge–B doped fibre and SMF-28 when exposed to 248 nm radiation is significantly higher.

It has previously been reported that the processes induced in the fibre by 248 nm radiation are different from those induced by 193 nm radiation.[49] In addition, it is thought that the exposure of optical fibre to UV increases the stress in the core. The results reinforce these concepts; they suggest that the 248 nm mechanism increases the internal core stress of the fibre significantly more than the 193 nm mechanism, such that 248 nm radiation causes a larger degradation of the fibre strength.

We have tested the fracture strength of FBG sensors fabricated by ourselves. In order to eliminate the mechanical strength degradation of the coating stripping, we decoated the coating of the fibre with acetone prior to UV laser exposure. The UV radiation was a laser operating at 193 nm. The light focused with a cylindrical lens then passed through a phase mask before irradiating the fibre. The frequency of the UV irradiation is 5 Hz.

Figure 8.6 shows the mechanical strength and the reflectivity of the FBG sensors. In the fracture strength test, the length of the gauge is 0.25 m and the strain rate is 1 mm/min. It can be seen that the mechanical strength of the

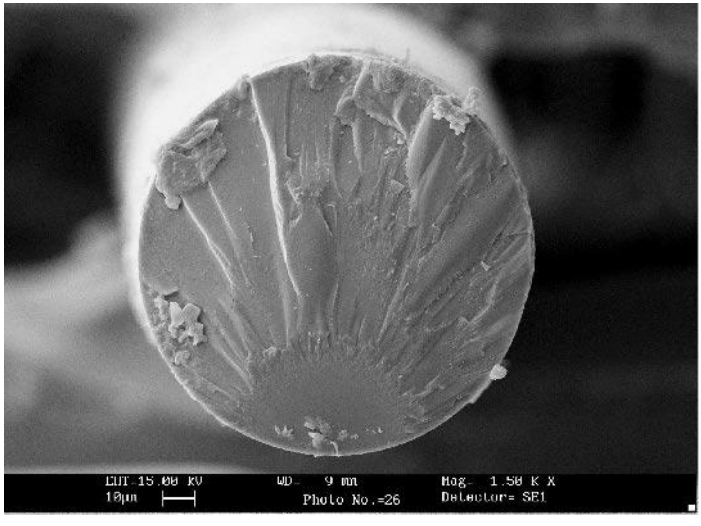

8.7 SEM of the cross-section of the broken grating. The start of the break is at the lower side. The UV laser is radiated from bottom to top.

FBG sensor degraded drastically with the increase in UV irradiation, and after a certain dose the mechanical strength will not degrade with the growth of UV irradiation. The strength of the FBG sensor is only about one-third of the optical fibre without UV irradiation. We can also see that the reflectivity increases sharply once the reflected peak appears, and then flattens as the UV irradiation increases. The strength degradation has been completed even before the reflected peak appears in our experiment, as if there were an obvious relation between the strength degradation and the reflectivity of the grating.

The SEM of the cross-section of the broken FBG sensor is shown in Fig. 8.7. The UV light irradiated the optical fibre from bottom to top. The beginning of the fracture was not always at the UV irradiation side, and the lateral side of optical fibre with UV irradiation was observed carefully with SEM; no flaw could be seen. This means the mechanical strength degradation takes place not only because of the flaws on the fibre surface induced by UV radiation. The mechanism of the mechanical strength degradation of the FBGs is not clear. Possibly, it is related to the structural change of the optical fibre molecule after UV irradiation.

Figure 8.8 is the comparison of the strength degradation with different irradiation energy/pulse at the same frequency. The strength degradation is larger with higher irradiation energy/pulse than with lower energy/pulse. This means that, in order to increase the mechanical strength of the FBGs, the

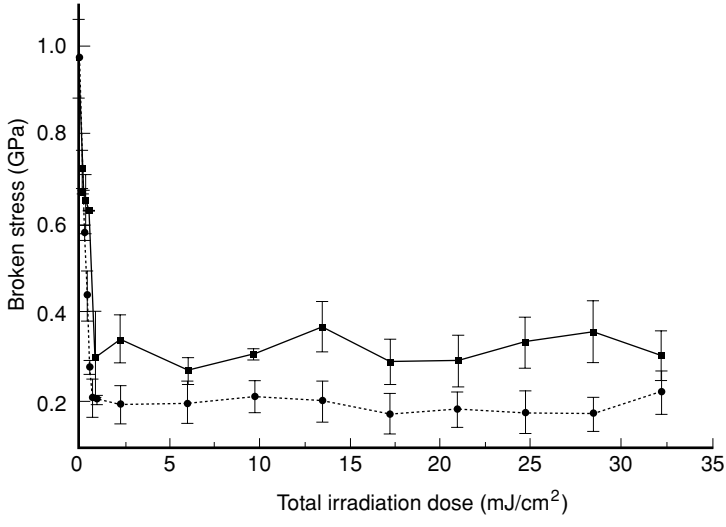

8.8 Strength degradation with different energy/pulse: —■— lower energy per pulse, ··· ● ··· higher energy per pulse.

irradiation energy/pulse should be lowered. We also observed that, not only does the reflectivity increase slowly with the growth of the total dose of UV irradiation after certain reflectivity (99%), but also the line-width of the reflected peak gets wider. The wide reflected peak is disadvantageous for the accuracy of the test. Thus, in FBG fabrication, the UV irradiation time should not be too long.

Because FBG fabrication is a complex procedure and glass fibre is brittle, the mechanical strength degradation is related not only to the UV irradiation but also to the coating stripping method. We have stripped coating with different methods in our FBG fabrication and compared their influence on the mechanical strength of the optical fibre. Optical fibres were divided into two groups, each with 20 samples. One group had the coating stripped with acetone, and the other with sulfuric acid. Coating stripped with acetone was a physical procedure. The stripped part of the optical fibre was soaked into acetone for several minutes, the acetone caused the costing to soften and swell; the coating then separated from the cladding. The coating can be pulled off gently. When the optical fibre was immersed in sulfuric acid (98%) at room temperature ($\sim 20\,^{\circ}C$), the coating was ablated by sulfuric acid, which took about 5 minutes. The optical fibre was then rinsed in water to remove the residual acid and other materials. No mechanical shock occurred to fibres in these two coating stripping procedures. The mechanical fracture during stripping was reduced to as little as possible. The mechanical strength of these stripped

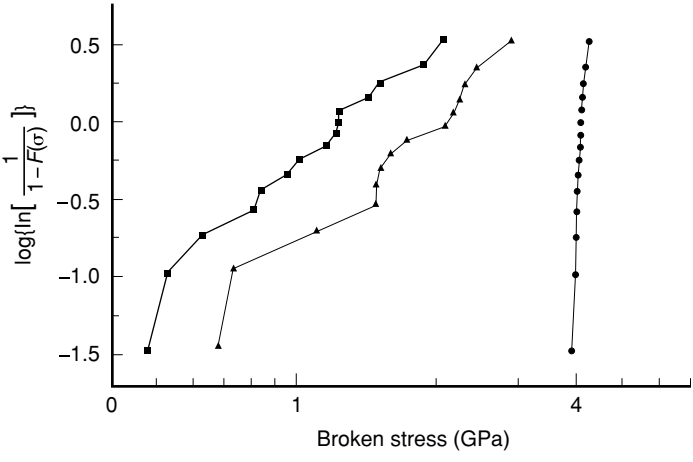

8.9 Weibull plot of optical fibre with different coating stripping method. —●— pristine fibre, —■— decoated with acetone, —▲— decoated with H_2SO_4.

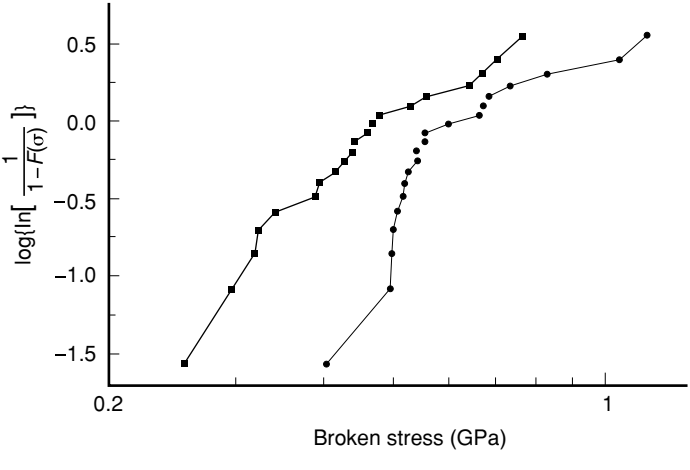

8.10 Influence of UV irradiation frequency on mechanical strength of FBGs. —■— 26 kV, 5 Hz, —●— 26 kV, 8 Hz.

optical fibres was tested. The Weibull plot is shown in Fig. 8.9. Table 8.2 gives the parameters for the distribution. The mechanical strength degraded notably when the coating was stripped with acetone. This may be related to the properties of these two solvents.

We have also compared the mechanical strength of FBGs fabricated with different frequencies of UV irradiation. The energy per pulse was the same

Table 8.2 Mechanical strength of optical fibre with different stripping method

	Stripped with acetone	Stripped with sulfuric acid	Pristine fibre
Mean of broken stress	1.14	1.76	4.09
Median stress	1.16	1.67	4.09
m value	2.8	2.8	52.0

Table 8.3 The influence of UV irradiation frequency

	Without UV irradiation	Grating	
		5 Hz	8 Hz
Mean of broken stress	1.76	0.47	0.63
Median stress	1.67	0.44	0.55
m value	2.8	4.0	4.1

Coating stripped with H_2SO_4.

with different frequencies. Figure 8.10 is the Weibull plot of FBGs with different UV irradiation. We can ascertain that the mechanical strength degradation is larger with lower frequency irradiation. As shown in Table 8.3, the *m*-values are almost the same in both situations and, obviously, the median broken strength of gratings with 8 Hz irradiation is higher than that of gratings fabricated with 5 Hz irradiation. This may be because irradiation with high frequency can increase the surface temperature of the fibre, resulting in the thermal annealing of some of the flaws produced in the first phase, thereby increasing the median break stress of the fibre.

We have also studied the influence of spot size on the mechanical strength. In FBG fabrication, we have found that when UV lasers pass through the phase mask, the density of light is not uniform. There was a notable change in the area of the edge of the phase mask. We have fabricated FBGs under different fabrication conditions and compared their mechanical strength. Group 1 was fabricated under normal fabrication conditions. The spot size is 27 mm × 1 mm. When Group 2 was fabricated, part of the UV light was covered so that the spot size was only within the mask area. The spot size was 9 mm × 1 mm. The edge effect of the phase mask was avoided. The Weibull plot of the FBG is shown in Fig. 8.11.

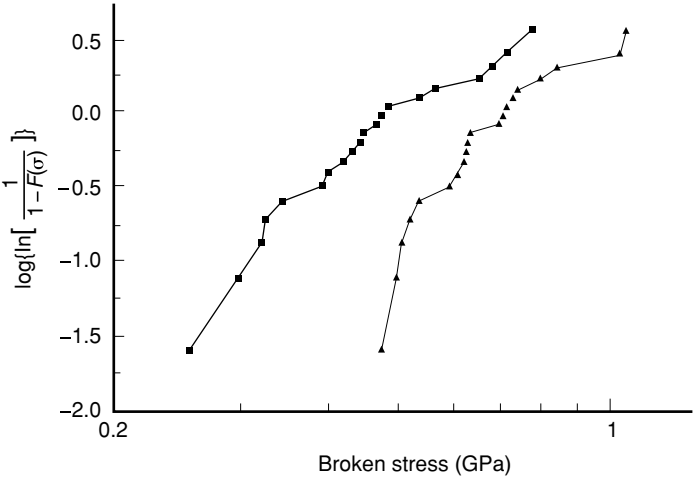

8.11 Weibull plot of FBGs with different spot size during fabrication: —■— 27 mm × 1 mm, —▲— 9 mm × 1 mm.

8.5.1.3 Enhancing the mechanical performance of FBG sensors

Because the strength degradation of the FBG sensors has important consequences for the reliability of the UV-induced Bragg gratings which are used as strain, temperature, and pressure sensors in a variety of fields, Varelas et al.[50,51] have examined the influence of homogeneous irradiation, using a continuous wave (CW) laser in the mechanical degradation of the fibre and compared it with the equivalent irradiation dose delivered by a pulsed laser source. Imamura et al.[52] have developed a new method for fabricating Bragg gratings with direct writing. The strength of Bragg gratings has been enhanced notably.

CW laser irradiation results in the mechanical resistance of a fibre being similar to that of a pristine fibre. This is in contrast to the case where the fibre undergoes pulse excimer irradiation. The total dose dependence is also less pronounced in the case of CW irradiation. This phenomenon has important consequences for Bragg grating fabrication, where high mechanical resistance is required for strain applications.

Although high strength Bragg gratings with higher reflectivity can be fabricated by CW UV exposure after chemical stripping of the protective polymer coating, this is not practical as it requires recoating and packaging. It has the potential for reducing the fibre strength due to exposure of the bare fibre to air. A direct fibre Bragg grating writing method through the coating has been demonstrated.[52,53] Imamura et al.[54] directly fabricated fibre gratings through the coating and have succeeded in producing a high strength fibre

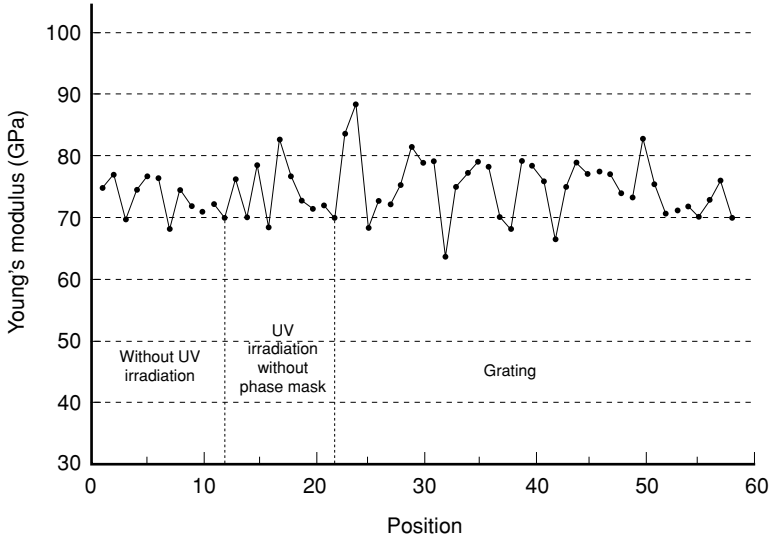

8.12 Young's modulus of the optical fibre.

grating. Tin-codoped germanosilicate fibre is more photosensitive than germanium-doped fibre.[55] The germanosilicate single mode fibre was codoped with 15 000 ppm Sn and 900 ppm Al in the core. To further enhance the fibre sensitivity, the fibres were treated under low temperature hydrogen for 2 weeks at 20 MPa prior to the UV exposure. The silica cladding had a diameter of 125 μm and was single coated with a UV-transparent UV-curable resin to an outer diameter of 200 μm.

8.5.2 Influence of UV irradiation on Young's modulus and hardness of fibre

The influence of UV irradiation on the mechanical strength of optical fibres is notable. How about the influence of UV irradiation to the other mechanical properties of optical fibres? Young's modulus and hardness of the optical fibre with and without UV irradiation have been tested using the Nano Indenter IIp.

In the test, the surface of the sample should be a smooth plane. The optical fibre is so thin that the lateral side has a large curvature. In order to get a plane in the lateral side of the optical fibre, the tested fibres were put into a polymer, then the polymer was polished carefully with lapping film (0.2 μm) so that a very smooth plane along the fibre was obtained. The sample contained three parts: optical fibre without UV irradiation, with UV irradiation but without phase mask, and grating. The result of Young's modulus of the cladding is

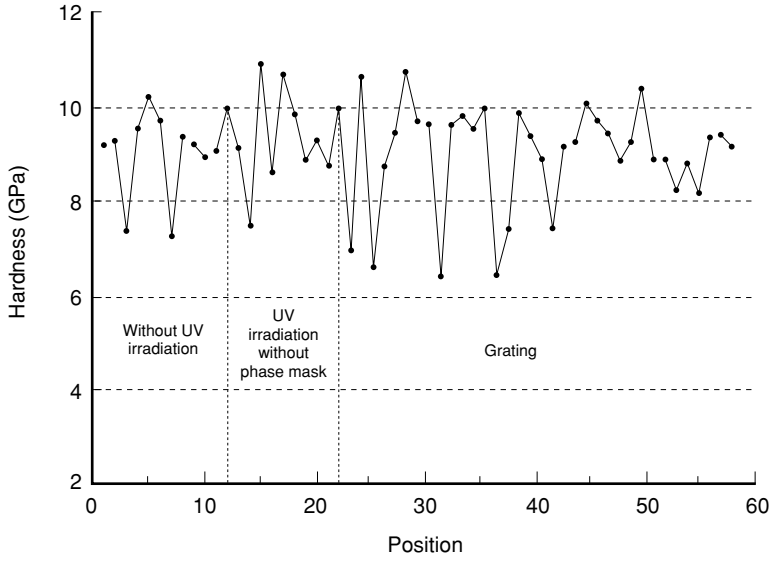

8.13 Hardness of the optical fibre.

shown in Fig. 8.12. There is no notable difference between the three parts. Statistical analysis[56] was performed. Suppose the measured data belong to normal distribution, with a 95% confidence level, the confidence interval of three parts are 71.29 GPa $< \mu <$ 75.30 GPa, 66.00 GPa $< \mu <$ 77.97 GPa and 73.28 GPa $< \mu <$ 76.76 GPa, respectively to optical fibre without UV irradiation, with UV irradiation without phase mask, and grating. They are almost in the same range. That is to say, the UV irradiation cannot influence Young's modulus of the optical fibre. Figure 8.13 is the hardness of the optical fibre. The UV irradiation cannot influence the hardness of the optical fibre either. Changing the depth of the plane (by polishing the tested fibre so that the test plane is closer to the core of the fibre), the results are the same.

From the experiment above we can confirm that it is reasonable to assume that the deformation of optical fibre contains uniform Bragg grating during the tension and the strain measured is believable.

8.6 Polymeric fibre

8.6.1 Properties of polymer optical fibre

Polymer optical fibre (POF) is a circular optical waveguide. POF is receiving increasing interest in short-distance communication systems because of its large power-carrying capacity, ease of joining and light weight. The structure

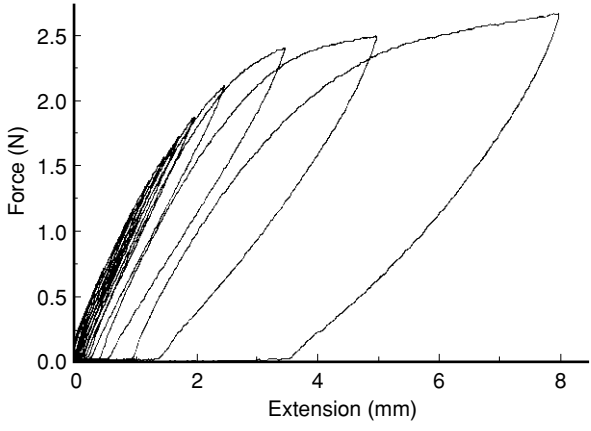

8.14 Extension properties of plastic optical fibre with ten cycles.

of POF is as the same as silica optical fibre. It consists of a central part, the core, with refractive index n_1 and of cylindrical shape, surrounded by a second part, the cladding, with a lower refractive index n_2. These two areas, which are essential for the light guiding, are composed of two different but transparent organic materials. In order to avoid external damage or the deterioration of this surface during the handling or use of the optical fibre, it is often covered with a protective coating which plays no part in the light guiding.

The core diameter varies according to the type of fibre, but is of the order of a millimetre, except in special cases. For economic reasons, the thickness of the cladding is much less, of the order of tens of micrometres. The surface of the core/cladding separation must be as even as possible.

A possible classification of POF can be based on the principal core material. The principal types of POF are fibres with PMMA (polymethyl methacrylate) core, fibres with PS (polystyrene) core, fibres with PC (polycarbonate) core and fibres with deuterated core.[57]

Physical properties, such as tensile resistance, compression resistance, shock resistance, torsion resistance, the effect of permanent winding, bending resistance, etc., temperature property and the chemical properties of POF have been studied systematically.[57]

8.6.1.1 The mechanical property

Figure 8.14 shows the elongation property of the measured fibre. In the measurement, the gauge length was 100 mm. The measurement was controlled by a programme, in which ten cycles were set. Each cycle contained loading and unloading; the speed was 0.5 mm/min. The elongation of the cycles was

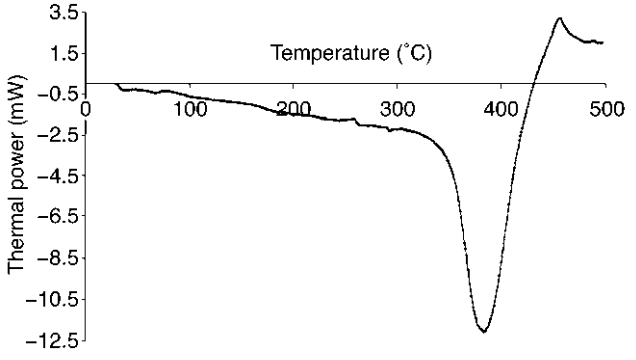

8.15 DSC of the sample of the plastic optical fibre.

0.5%, 1.0%, 1.25%, 1.5%, 1.75%, 2%, 2.5%, 3.5%, 5% and 8%, respectively. In this figure, the unloading curves were not the same as the loading curves. Like plastic material, the fibre has the hysteresis property. In the meantime, we find that, if the elongation of the fibre is larger than 1.5%, the sample cannot return to its original length even when the external force is released: this means that permanent deformation was induced in the sample. Sonic modulus was measured as 6.3 GPa.

8.6.1.2 DSC results

The heat flow to a sample can be measured in thermally controlled conditions with differential scanning calorimetry (DSC) by Mettler TA4000 Thermal Analysis System. The DSC measurement result is shown in Fig. 8.15. At 67.5 °C, some physical properties of the fibre were changed. This temperature is called the glass transition temperature. At 330 °C, the fibre began to melt. At 384.3 °C, the fibre began to be oxygenated, and it was completely oxygenated at 456.9 °C.

8.6.2 Bragg grating of polymer optical fibre

Although silica optical fibre Bragg gratings can be used to measure many physical parameters, the changes in the Bragg wavelength due to the change of these measured values are small. The measured range is limited, typically a few nanometres.[58] This is because silica glass has a small thermal effect and large Young's modulus. In the case of polymer optical fibre, the situation is different. Its Young's modulus (1 GPa), for example, is more than 70 times smaller than that of glass (72.9 GPa), and its elongation is much larger than that of glass

optical fibre. The refractive index changes that can be induced by photoreaction are relatively high ($\Delta n \sim 10^{-2}$). Therefore, it is expected that a Bragg grating written into a polymer optical fibre would be tunable over a very wide wavelength range. In addition, polymer optical fibre gratings are ideal devices for inclusion in an organic solid-state fibre laser,[59] which in turn provides a compact and low-cost optical source over a broad range of wavelengths throughout the visible spectrum.[60]

Xiong et al. have fabricated a photosensitive polymer optical fibre, whose refractive index in the core region can be changed under irradiation from a pulse UV laser beam, and have shown that it is possible to write gratings in these fibres.[61] They have fabricated several types of grating, including surface gratings on the flat surface of a preform, gratings in preform core, and gratings in the core of a multimode polymer optical fibre.

The polymer preform was prepared according to the method reported in Peng et al.,[62] except that the core monomer used contained a much lower level of lauryl peroxide and chain transfer agent so as to increase its photosensitivity. The preform was then cut into a square block with the core exposed and polished. A grating was fabricated by means of a phase mask with a period of 1.06 μm. The illumination period was 10 ns, and the pulse energy was about 5 mJ. The grating created at wavelength 248 nm was a surface grating formed by period removal of the core polymer. An atomic force microscope (AFM) was used to obtained a surface profile which has a grating period of 1.06 μm, coinciding with that of the pulse mask. The diffraction efficiency is 15%.

The mechanisms responsible for the formation of periodic structures in polymers have been explained.[63–65] They can be classified into photolysis, oxidization and laser ablation for the surface relief gratings, while chain scission, cross-link and photopolymerization are considered to be responsible for bulk or volume gratings and in-fibre gratings. The cross-link in Bragg grating fabrication can be shown as:

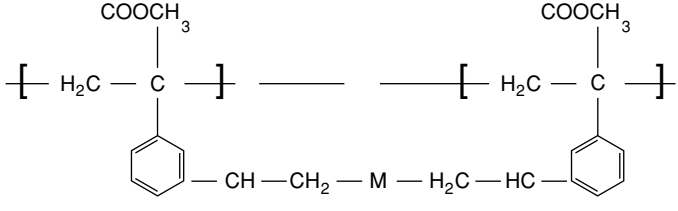

Peng et al. have written Bragg gratings in single-mode polymer optical fibre[66] and have shown that these gratings can be readily tuned over a wavelength range of 12 nm without changing their reflection spectra.

8.7 Conclusions

The mechanism and procedure of FBG fabrication are discussed, and the influences of UV irradiation on the mechanical strength of optical fibres are studied. The mechanical strength of optical fibres is unaffected by the on-line writing of a single pulse during fibre drawing. The strength degrades drastically with UV irradiation after the coating is stripped, and will degrade further with 248 nm single pulse UV irradiation than with 193 nm. The strength degradation is more serious with higher radiation energy per pulse than lower radiation energy. Lower UV irradiation frequency degrades the mechanical strength more than higher frequency. The mechanical strength of the optical fibre will not be lowered significantly after certain doses of UV irradiation. The mechanical strength of the FBG sensor can be increased notably with CW UV irradiation and the direct writing method without stripping the coating. Young's modulus and the hardness of the optical fibre will not change with UV irradiation.

Because of its large elongation property and relatively high refractive index changes induced by photoreaction, a Bragg grating written into a plastic optical fibre would be tunable over a very wide wavelength range. Plastic FBGs can be used to measure large strain and other physical properties with a large change range of structures.

Acknowledgements

The authors wish to acknowledge Hong Kong Research Grants Council for supporting this work (Grant No Polyu5112/98E) and Dr Dongxiao Yang for conducting the measurement of PMMA optical fibres.

References

1 Hill K, Fujii Y, Johnson D C and Kawasaki B S, 'Photosensitivity in optical fibre wave guide applications to reflection filter fabrication', *Appl. Phys. Lett*., 1978, **32**, 647–9.
2 Kawasaki B S, Hill K O, Johnson C D and Fujii Y, 'Narrow-band Bragg reflectors in optical fibres', *Opt. Lett*., 1978, **3**, 66–8.
3 Meltz G, Morey W W and Glenn W H, 'Forming of Bragg grating in optical fibres by a transverse holographic method', *Opt. Lett*., 1989, **14**, 823–5.
4 Askins C C, Putnam M A, Williams G M and Friebele E J, 'Stepped-wavelength optical-fibre Bragg grating arrays fabricated in line on a draw tower', *Opt. Lett*., 1994, **14**, 823–4.
5 Archambault J L, Reekie L and Russell, 'High reflectivity and narrow bandwidth fibre grating written by single excimer pulse', *Electron. Lett*., 1993, **29**, 28–9.

6 Kersey A D, 'Interrogation and multiplexing techniques for fibre Bragg grating strain-sensors', *Proc. SPIE*, 1993, **2071**, 30–48.
7 Rao Y J, 'In fibre Bragg grating sensors', *Meas. Sci. Technol*., 1997, **8**, 355–75.
8 Mather M H, Tabrizi K, Prohaska J D and Snitzer E, 'Fibre Bragg gratings for civil engineering applications', *Proc. SPIE*, 1996, **2682**, 298–302.
9 Friebele E J, Askins C G, Putnam M A et al., 'Distributed strain sensing with fibre Bragg grating arrays embedded in CRTM™ composite', *Electron. Lett*., 1994, **30**, 1783–1784.
10 Friebele E J, Askins C G, Putnam M A et al., 'Demonstration of distributed strain sensing in production scale instrumented structures', *Proc. SPIE*, 1996, **2721**, 118–24.
11 Bullock D E, Dunphy J R, Hufstetler G H, 'Embedded Bragg grating fibre optic sensor for composite flexbeams', *Proc. SPIE*, 1993, **1789**, 253–61.
12 Chen B X, Mather M H and Nawy E G, 'Fibre-optic Bragg grating sensor for nondestructive evaluation of composite beam', *J. Struct. Eng*., 1994, **12**(12), 3456–70.
13 Measures R M, Alavie A T, Maaskant R, Ohn M, Karr S and Huang S, 'Structurally integrated Bragg grating laser sensing system for a carbon fibre pre-stressed concrete highway bridge', *Smart Mater. Struct*., 1995, **4**(1), 20–30.
14 Du W C, Tao X M, Tam H Y and Choy C L, 'Optical Bragg grating sensors in smart textile structural composite', *Proceeding of the 4th International Conference on Composite Engineering*, *ICCE/4*, Hawaii, USA, 1997, 289–90.
15 Ferdinand P, Ferragu O, Lechien J L et al. 'Mine operating accurate stability control with optical fibre sensing and Bragg grating technology: the European brite/euram stabilos project', *J. Lightwave Technol*., 1995, **13**, 1303–12.
16 Rao Y J, Jackson D A, Zhang L and Bennion I, 'In-fibre Bragg grating temperature sensor system for medical applications', *J. Lightwave Technol*., 1997, **15**, 779–85.
17 Griffioen W, 'Mechanical life time model for optical fibre in water', *Proc. SPIE*, 1994, **2074**, 2–10.
18 Haslove P, Jensen K B and Skovgaard N H, 'Degradation of stressed optical fibres in water: new worst case lifetime estimation model', *J. Am. Ceram. Soc*., 1994, **77**, 1531–40.
19 Bouten P C P and Broer D J, 'Coating composition and fibre life time', *Proc. SPIE*, 1994, **2074**, 59–64.
20 Inniss D, Brownlow D L and Kurkjian C R, 'Chemical effects on the fatigue of light-guide fibres', *Proc. SPIE*, 1992, **1791**, 3–10.
21 Wei T, Yuee H H, Hasz C H and Key P L, 'Degradation of fibre strength during coating stripping', *Int. Wire and Cable Symp. Proc*., 1989, 199–204.
22 Rondinella V V and Matthewson M J, 'Effect of chemical stripping on the strength and surface morphology of fused silica fibre', *Proc. SPIE*, 1994, **2074**, 52–8.
23 Damsgaard H and Hansen O, 'Factory spliced fibres: technology, performance and field experience', *Int. Wire and Cable Symp. Proc*., 1990, 284–90.
24 Olshansky R and Maurer D R, 'Tensile strength and fatigue of optical fibres', *J. Appl. Phys*., 1976, **47**(10), 4497–9.
25 Mitsunaga Y, Katsuyama Y and Ishida Y, 'Reliability assurance for long-length optical fibre based on proof testing', *Electron. Lett*., 1981, **17**, 568–71.
26 Griffioen W, Breuls T, Cocito G, Dodd S, Ferri G, Haslov P, Oksanen L, Stockon D and Svensson T, 'COST 218 evaluation of optical fibre lifetime models', *Proc. SPIE*, 1992, **1791**, 190–5.

27 Friebele E J, Griscom D L and Siegal G H Jr, 'Defect centers in germania doped silica optical fibre', *J. Appl. Phys.*, 1974, **45**, 3424–8.
28 Kawazoe H, 'Effects of modes of glass formation on the structure of intrinsic or photoinduced defects centered on III, IV, or V cations in oxide glasses', *J. Non-cryst. Solids*, 1985, **71**, 213–34.
29 Tsai T E, Griscom D L, Friebele E J and Fleming J W, 'Radiation induced defect centers in high purity GeO_2 glass', *J. Appl. Phys.*, 1987, **62**, 2262–8.
30 Griscom D L and Mizuguchi M, 'Determination of the visible range optical absorption spectrum of peroxy radicals in gamma irradiation fused silica'. In *Bragg Gratings, Photosensitivity and Poling in Glass Fibres and Waveguides: Fundamentals and Applications*, 1997 OSA Technical Digest Series, **17**, Paper JMD2, 139–41.
31 Honso H, Abe Y, Kinser D L, Weeks R A, Muta K and Kawazoe H, 'Nature and origin of the 5eV band in SiO_2:GeO_2 glasses', *Phys. Rev. B*, 1995, **46**, II-445–II-451.
32 Tsai T E and Friebele E J, 'Kinetics of defects centers formation in Ge–SiO_2 fibre of various compositions'. In *Bragg Gratings, Photosensitivity and Poling in Glass Fibres and Waveguides: Fundamentals and Applications*, 1997, OSA Technical Digest Series, **17**, Paper JMD2, 101–3.
33 Hand D P and Russel P St J, 'Photoinduced refractive index changes in germanosilicate optical fibres', *Opt. Lett.*, 1990, **15**(2), 102–4.
34 Williams D L, Davey S T, Kashyap R, Armitage J R and Ainslie B J, 'Direct observation of UV-induced bleaching of 240 nm absorption band in photosensitive germanosilicate glass fibres', *Electron. Lett.*, 1992, **28**(4), 369–71.
35 Riant I, Borne S and Sansonetti P, 'Evidence of densification in UV-write Bragg gratings in fibres'. In *Photosensitivity and Quadratic Nonlinearity in Waveguides: Fundamentals and Applications*, 1995, **22**, 51–5.
36 Poumellec B, Guenot P, Riant I et al., 'UV induced densification during Bragg grating inscription in Ge:SiO_2 preforms', *Opt. Mater.*, 1995, **4**, 441–9.
37 Bernardin J P and Lawandy N M, 'Dynamics of the formation of Bragg gratings in germanosilicate optical fibres', *Opt. Commun.*, 1990, **79**, 194–8.
38 Rothschild M, Erlich D J and Shaver D C, 'Effects of excimer irradiation on the transmission, index of refraction, and density of ultraviolet grade fused silica', *Appl. Phys. Lett.*, 1989, **55**(13), 1276–8.
39 Douay M, Ramecourt D, Tanuay T et al. 'Microscopic investigations of Bragg gratings photo-written in germanosillicate fibres'. In *Photosensitive and Quadratic Nonlinearity in Waveguides: Fundamentals and Applications*, 1995, OSA Technical Digest Series, **22**, 48–51.
40 Fonjallaz P Y, Limberger H G, Salathe, Cochet F and Leuenberger B, 'Tension increase correlated to refractive index change in fibres containing UV written Bragg gratings', *Opt. Lett.*, 1995, **20**(1), 1346–8.
41 Griffith A A, 'The phenomena of rupture and flaw in solids', *Phil. Trans. Roy. Soc.*, 1920, **221A**, 163–9.
42 Kurkjian C R and Paek U C, 'Single value strength of perfect silica fibres', *Appl. Phys. Lett.*, 1983, **42**, 251–3.
43 Oliver W C and Pharr G M, 'An improved technique for determining hardness and elastic modulus using load and displacement sensing indentation experiments', *J. Mater. Res.*, 1992, **7**(6), 1564–83.
44 Sneddon I N, 'The relation between load and penetration in the axisymmetric

boussinesq problem for a punch of arbitrary profile', *Int. J. Engng. Sci.*, 1965, **3**, 47–57.
45 Askins C G, Putnam M A, Williams G M and Friebele E J, 'Stepped-wavelength optical fibre Bragg grating arrays fabricated in line on a draw tower', *Opt. Lett.*, 1994, **19**(2), 147–9.
46 Askins C G, Putnam H J, Patrick H J and Friebele E J, 'Fibre strength unaffected by on-line writing of single-pulse Bragg grating', *Electron. Lett.*, 1997, **33**(15), 1333–4.
47 Hagemann V, Trutzel M N, Staudigel L, Rothhardt M, Muller H-R and Krumpholz O, 'Mechanical resistance of draw-tower-Bragg grating sensors', *Electron. Lett.*, 1998, **34**(2), 211–12.
48 Feced R, Roe-Edwards M P, Kanellopoulos S E, Taylor N H and Handerick V A, 'Mechanical strength degration of UV exposed optical fibres', *Electron Lett.*, 1997, **33**(2), 157–9.
49 Albert J, Malo B, Hill K O, Bilodeau F, Johnson D C and Theriault S, 'Comparison of one-photon and two-photon effects in photosensitivity of germanium-doped silica optical fibres exposed to intense ArF excimer laser pulses', *Appl. Phys. Lett.*, 1995, **67**(24), 3529–31.
50 Varelas D, Limberger H G, Salathe R P and Kotrotsios C, 'UV-induced mechanical degradation of optical fibres', *Electron. Lett.*, 1997, **33**(9), 804–5.
51 Varelas D, Limberger H G and Salathe R P, 'Enhanced mechanical performance of single mode optical fibres irradiated by a CW UV laser', *Electron. Lett.*, 1997, **33**(8), 704–5.
52 Imamura K, Nakai T, Moriura K, Sudo Y and Imada Y, 'Mechanical strength characteristics of tin-codoped germanosilicate fibre Bragg gratings fabricated by writing through UV-transparent coating', *Electron. Lett.*, 1998, **34**(10), 1016–17.
53 Chao L, Reekie L and Ibsen M, 'Grating writing through fibre coating at 244 and 248 nm', *Electron. Lett.*, 1999, **35**(11), 924–5.
54 Imamura K, Nakai T, Sudo Y and Imada Y, 'High reliability of tin-codoped germanosilicate fibre Bragg gratings fabricated by direct writing method', *Electron. Lett.*, 1998, **34**(18), 1772–4.
55 Dong L, Cruz J L, Reekie L, Xu M G and Payne D N, 'Enhanced photosensitivity in tin-codoped germansilicate optical fibres', *IEEE Photon. Technol. Lett.*, 1995, **7**, 1048–50.
56 Sanders D H, *Statistics*: *A Fresh Approach*, McGraw-Hill, Inc., 1990.
57 Marcou J (ed.), *Plastic Optical Fibres*: *Practices and Applications*, John Wiley, New York, 1997.
58 Hill K O and Meltz G, 'Fibre Bragg grating technology fundamental and overview', *J. Lightwave Technol.*, 1997, **15**(8), 1263–76.
59 Kaminov I P, Weber H P and Chandross E A, 'Poly(methyl methacrylate) dye laser with internal diffraction grating resonator', *Appl. Phys. Lett.*, 1971, **18**, 497–9.
60 Dodabalapur A, Chandross E A, Berggren M and Slusher R E, 'Organic solid-state lasers: past and future', *Science*, 1997, **277**, 1787–8.
61 Peng G D, Xiong Z and Chu P L, 'Photosensitivity and gratings in dye-doped polymer optical fibres', *Optical Fibre Technol.*, 1999, **5**(2), 242–51.
62 Peng G D, Chu P L, Xiong Z, Whitbread T and Chaplin R P, 'Dye-doped step-index polymer optical for broadband optical amplification', *J. Lightwave Technol.*, 1996, **14**, 2215–23.
63 Tomlinson W J, Kaminow I P, Chandross A, Fork R L, and Silfvast W T,

'Photoinduced refractive index increase in poly(methylmethacrylate) and its applications', *Appl. Phys. Lett*., 1970, **16**, 486–9.
64 Bolle M, Lazare S, Blanc M L and Wilmes A, 'Submicron periodic structures produced on polymer surfaces with polarized excimer laser ultraviolet radiation', *Appl. Phys. Lett*., 1992, **60**, 674–6.
65 Decker C, 'The use of UV irradiation in polymerization', *Polymer Int*., 1998, **45**, 133–7.
66 Xiong Z, Peng G D, Wu B and Chu P L, 'Highly tunable Bragg gratings in single-mode polymer optical fibres', *IEEE Photon. Technol. Lett*., 1999, **11**(3), 352–4.

9

Optical responses of FBG sensors under deformations

DONGXIAO YANG, XIAOMING TAO AND APING ZHANG

9.1 Introduction

Many sensors[1–16] can be used to measure the strain and deformations, such as traditional strain-meter sensors, piezoelectric sensors, piezo-resistive sensors, optic sensors based on fluorescence spectroscopy or Raman spectroscopy, fibre optic sensors based on Brillouin scattering, fibre optic sensors based on interferometer or/and polarimeter, fibre optic sensors based on photography and fibre Bragg grating (FBG) sensors. FBG sensors have been considered excellent sensing elements, suitable for measuring static and dynamic fields, like temperature, strain and pressure. Since the measured information is wavelength encoded,[13–22] FBG makes the sensor self-referencing, rendering it independent of fluctuating light levels and the system immune to source power and connector losses that plague many other types of fibre optic sensors. The advantages of FBG sensors include light weight, flexibility, stability, potential low cost, longer lifetime, higher temperature capacity, unique wavelength-multiplexing capacity, suitable size for embedding into composites without introducing significant perturbation to the characteristics of the structure, good invulnerability to electro-magnetic interference, and even durability against high radiation environments, making reproducible measurements possible. Therefore, FBG sensors seem to be ideal for realizing fibre optic smart structures where sensors are embedded in or attached to structures for achieving a number of technical objectives, such as health monitoring, impact detection, shape control and vibration damping, via the provision of real-time sensing information, such as strain, temperature and vibration. FBG sensors have been used for measurements of a wide variety of parameters: some FBG sensor systems have been installed in large-scale practical applications, and some are commercially available.[16] FBG sensors have been used in bridges, highways, textiles, mines, marine vehicles, medical therapies and aircrafts.[16,23–35] They[13,14,36–74] can be used for quasi-static strain monitoring, dynamic strain sensing, time- and wavelength-division multiplexing, and temperature/strain

discrimination. The combination of FBG and long period fibre grating can be used to simultaneously determine strain and temperature. FBGs can also be used in laser sensors and interferometer sensors.

Most of the sensing applications of FBG sensors focus on its reflection spectra, which depend on the relationship between the Bragg wavelength of FBG and its physical quantities.[13,14] The key detection issue is the determination of the often small measurand-induced Bragg wavelength shift. In addition to fibre grating spectra, the polarization optics of FBG sensors will also be discussed in this chapter. The contents include optical methodologies, optical responses under tension, torsion, lateral compression and bending.

9.2 Optical methodology for FBG sensors

An optical fibre is a cylindrical dielectric waveguide made of low-loss materials such as silica glass. It has a central core in which the light is guided, embedded in an outer cladding of slightly lower refractive index. Light rays incident on the core-cladding boundary at angles greater than the critical angle undergo total internal reflection and are guided through the core without refraction. Rays of greater inclination to the fibre axis lose part of their power into the cladding at each reflection and are not guided.

Light in fibre propagates in the form of modes. In mathematics, a mode in optic fibre is a solution of the Maxwell's equations under the boundary conditions. The guided modes are electric and magnetic fields that maintain the same transverse distribution and polarization at all distances along the fibre axis. Each mode travels along the axis of the fibre with a distinct propagation constant and group velocity, maintaining its transverse spatial distribution and its polarization. There are two independent configurations of electric and magnetic vectors for each mode, corresponding to two states of polarization. When the core diameter is small, only a single mode is permitted and the fibre is said to be a single mode fibre. Fibres with large core diameters are multimode fibres.

9.2.1 Electric field in single mode fibre

In a single mode fibre, the weakly guiding approximation $n_{co} - n_{cl} \ll 1$ is satisfied, where n_{co} and n_{cl} are the refractive index of the core and the cladding, respectively. The fundamental mode is hybrid mode HE_{11}, which can be simplified in the analysis by linear polarized mode LP_{01}. This fundamental mode consists of two orthogonal modes HE_{11}^{x} and HE_{11}^{y} in accordance with their polarization directions, so the electric fields in a single mode fibre which is not under Bragg condition can be well represented as:

$$\boldsymbol{E}(x, y, z; t) = \sum_{m=1}^{2} c_m(z)\mathbf{E}_m(x, y)\exp[-i(\omega t - \beta_m z)] \quad [9.1]$$

where c_1 and c_2 denote the slowly varying amplitudes of the orthogonal HE_{11} modes, ω, β_1, β_2, $\mathbf{E}_1$ and $\mathbf{E}_2$ are the angular frequency, the propagation constants of HE_{11}^x, and HE_{11}^y, the transverse spatial distribution of electric field HE_{11}^x, and the transverse spatial distribution of electric field HE_{11}^y, respectively, and

$$\mathbf{E}_1(x, y) = F_0(r)\boldsymbol{e}_x + (i/\beta_0)\cos\theta[\mathrm{d}F_0(r)/\mathrm{d}r]\boldsymbol{e}_z \quad [9.2]$$

$$\mathbf{E}_2(x, y) = F_0(r)\boldsymbol{e}_y + (i/\beta_0)\sin\theta[\mathrm{d}F_0(r)/\mathrm{d}r]\boldsymbol{e}_z \quad [9.3]$$

where $F_0(r)$ represent the zero-order Bessel functions J_0 in the core, and modified Bessel functions K_0 in the cladding, respectively, β_0, $\boldsymbol{e}_x$, $\boldsymbol{e}_y$ and $\boldsymbol{e}_z$ are the propagation constant of the mode in an ideal single mode fibre, the unit vectors in x, y and z directions, respectively.

The coupled mode theory is often used to describe the polarization characteristics, or modes coupling in optical fibre, and the reflection spectra of FBG sensors. When the optical response of an optical fibre is analysed based on the coupled mode theory, the electric field is normalized as $\int\int \mathbf{E}_{nt} \cdot \mathbf{E}_{nt}^* \mathrm{d}x\mathrm{d}y = 1$. Based on the perturbation approach, the slowly varying amplitudes c_m are determined by the following coupled mode equations:

$$\mathrm{d}c_1(z)/\mathrm{d}z = i\{\kappa_{11}c_1(z) + \kappa_{12}c_2(z)\exp[(\beta_2 - \beta_1)z]\} \quad [9.4]$$

$$\mathrm{d}c_2(z)/\mathrm{d}z = i\{\kappa_{21}c_1(z)\exp[-(\beta_2 - \beta_1)z] + \kappa_{22}c_2(z)\} \quad [9.5]$$

where the subscripts 1 and 2 denote the modes HE_{11}^x and HE_{11}^y, respectively. The amplitude coupling coefficient from mode m to mode n is given by:

$$\kappa_{nm} = (k_0^2/2\beta_0)\int\int(\tilde{\varepsilon}_{ij}\mathbf{E}_m) \cdot \mathbf{E}_n^* \mathrm{d}x\mathrm{d}y, \qquad n, m = 1, 2 \quad [9.6]$$

where $\tilde{\varepsilon}_{ij}$ is the dielectric permittivity perturbation tensor.

9.2.2 Polarization optics[75–81]

When the polarization behaviour of FBGs under various deformations is discussed, one has to consider three types of perturbation, that is, those induced by the fibre making process (intrinsic), UV side exposure and strain caused by deformation.

An evolution velocity Ω is usually introduced to describe qualitatively the polarization characteristics of specific polarization behaviour. Ω in a generalized Poincaré sphere can be expressed by the coupled coefficients as:[77]

$$|\Omega| = [(\kappa_{11} - \kappa_{22})^2 + 4\kappa_{12}\kappa_{21}]^{1/2} \quad [9.7]$$

$$2\chi = \arg(\kappa_{11} + \kappa_{12} - \kappa_{21} - \kappa_{22}) \quad [9.8]$$

$$2\psi = \arctan[(\kappa_{11} - \kappa_{22})/(4\kappa_{12}\kappa_{21})]^{1/2} \quad [9.9]$$

where 2χ and 2ψ are the latitude and longitude of the generalized Poincaré sphere, respectively. Hence the general approach of the polarization analysis based on the coupled mode theory is used, by analysing the permittivity perturbation first, then inserting it into the coupled mode equations, obtaining the solutions of c_1 and c_2, and qualitatively presenting the polarization characteristics by the evolution velocity.

The Poincaré sphere,[75] which has a unit radius and the spherical angular coordinates 2ψ (longitude) and 2χ (latitude), is often used to represent the different states of polarization geometrically. According to the traditional terminology which is based on the apparent behaviour of the electric vector when 'viewed' face on by the observer, we say that the polarization is right-handed when to an observer looking in the direction from which the light is coming, the end point of the electric vector would appear to describe the ellipse in the clockwise sense. Hence right-handed polarization is represented by points on the Poincaré sphere which lie below the equatorial plane, and left-handed by points on the Poincaré sphere which lie above this plane. Linear polarization is represented by points on the equator. Right- and left-handed circular polarization are represented by the south and north pole on the Poincaré sphere, respectively.

9.2.3 Reflection spectra

A fibre Bragg grating (FBG) consists of a periodic modulation of refractive index in the core of a single mode fibre. The electric fields in FBGs are represented by the superposition of the ideal modes travelling in both forward and backward directions:

$$\boldsymbol{E}(x, y, z; t) = \sum_k [a_k(z)\exp(i\beta_k z) + b_k(z)\exp(-i\beta_k z)]\mathbf{E}_k(x, y)\exp(-i\omega t) \quad [9.10]$$

where a_k and b_k are slowly varying amplitudes of the kth mode travelling in the $+z$ and $-z$ directions. The transverse mode fields $\mathbf{E}_k(x, y)$ might describe the LP modes, or the cladding modes. The modes are orthogonal in an ideal waveguide, hence do not exchange energy. The presence of a dielectric perturbation causes them to be coupled. Based on the slowly varying envelope approximation, the coupled mode equations for amplitudes a_k and b_k can be obtained by:

$$\frac{\mathrm{d}a_j(z)}{\mathrm{d}z} = i\sum_k (\kappa_{jk}^t + \kappa_{jk}^z)a_k(z)\exp[i(\beta_k - \beta_j)z] + i\sum_k (\kappa_{jk}^t - \kappa_{jk}^z)b_k(z)\exp[-i(\beta_k + \beta_j)z] \quad [9.11]$$

$$\frac{\mathrm{d}b_j(z)}{\mathrm{d}z} = -i\sum_k (\kappa_{jk}^t - \kappa_{jk}^z)a_k(z)\exp[i(\beta_k + \beta_j)z] - i\sum_k (\kappa_{jk}^t + \kappa_{jk}^z)b_k(z)\exp[-i(\beta_k - \beta_j)z] \quad [9.12]$$

where the transverse coupling coefficients between modes k and j are given by:

$$\kappa_{jk}^t = \frac{k_0^2}{2\beta_j}\int_{\infty}\int (\tilde{\varepsilon}_r \mathbf{E}_k)_t \cdot \mathbf{E}_{jt}^* \,\mathrm{d}x\mathrm{d}y \quad [9.13]$$

where $\tilde{\varepsilon}_r$ is the permittivity perturbation. It is often treated as a scalar term for FBG sensors, and can be approximately expressed by index perturbation as $\tilde{\varepsilon}_r \approx 2n \cdot \delta n$. However, in the cases where there is significant linear birefringence in an optical fibre, such as in polarization maintaining fibre, or under high lateral compression, it should be corrected. The longitudinal coefficient κ_{jk}^z can usually be neglected, since generally $\kappa_{jk}^z \ll \kappa_{jk}^t$ for modes. In most FBGs, the induced index change is non-existent outside the core, and the core refractive index changes can be expressed as:

$$\delta n = \delta n_{\mathrm{eff}}(z)\left\{1 + \eta \cdot \cos\left[\frac{2\pi}{\Lambda}z + \phi(z)\right]\right\} \quad [9.14]$$

where $\delta n_{\mathrm{eff}}(z)$ is the DC index change spatially averaged over a grating period, η is the fringe visibility of the index change, Λ is the nominal period, and $\phi(z)$ describes the grating chirp, respectively. Figure 9.1 shows some reflection spectra of normal FGBs with different fringe visibility.

If we insert the perturbation term Eq. (9.14) into Eq. (9.13), we can obtain quantitative information about the reflection spectra of fibre gratings. One of the most important results of FBGs is the phase-matching condition, or Bragg condition. The phase-matching condition of FBGs with period Λ is given by $\beta_1 - \beta_2 = 2\pi/\Lambda$, where β_1 and β_2 are the propagation constants of forward and backward propagation modes. $\beta_1 = -\beta_2 = \beta$ for directional coupling between the same modes. The phase-matching condition can then be simplified to $\beta = \pi/\Lambda$. If the effective refractive index is used to represent the propagation characteristics as $\beta = 2\pi \cdot n_{\mathrm{eff}}/\lambda$, it can then be expressed as:

$$\lambda_{\mathrm{B}} = 2n_{\mathrm{eff}}\Lambda \quad [9.15]$$

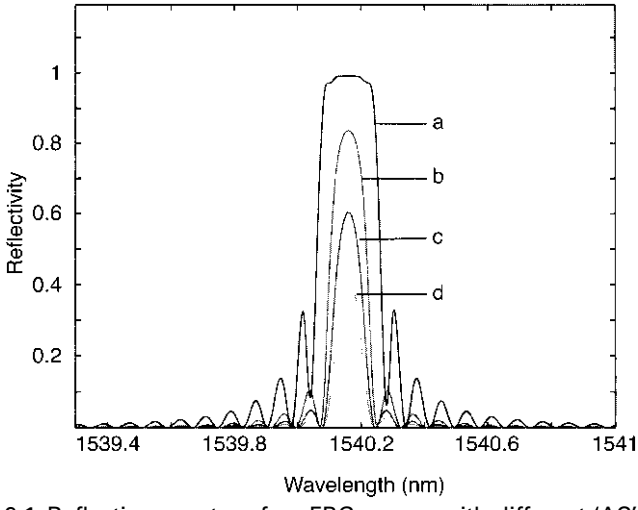

9.1 Reflection spectra of an FBG sensor with different 'AC' modulation dose (a) 2.0×10^{-4}; (b) 1.0×10^{-4}; (c) 0.67×10^{-4}; (d) 0.5×10^{-4}).

where the Bragg wavelength λ_B is the free space centre wavelength of the input light that will be back-reflected from the Bragg grating. Equation (9.15) is the first-order Bragg condition of the grating.

This first-order Bragg condition is simply the requirement that satisfies both energy and momentum conservation. Energy conservation requires that the frequencies of the incident radiation and the scattered radiation are the same, $\hbar\omega_s = \hbar\omega_i$, where $\hbar = h/2\pi$, h is Planck's constant, and ω_i and ω_s are radian frequencies of incident radiation and scattered radiation, respectively. Momentum conservation requires that the incident wave-vector $\boldsymbol{k}_i$, plus the FBG wave-vector $\boldsymbol{k}_g$, equal the wave-vector of the scattered radiation $\boldsymbol{k}_s = \boldsymbol{k}_i + \boldsymbol{k}_g$, where $\boldsymbol{k}_g$ has a direction normal to the FBG planes with a magnitude $2\pi/\Lambda$, Λ is the spacing period of the FBG, $\boldsymbol{k}_i$ has a direction along the propagation direction of the incident radiation with a magnitude $2\pi n_{eff}/\lambda_i$, λ_i is the free space wavelength of the incident radiation, n_{eff} is the modal index (the effective refractive index of the fibre core) at the free space wavelength, $\boldsymbol{k}_s$ has a direction along the propagation direction of the scattered radiation with a magnitude $2\pi n_{eff}/\lambda_s$, and λ_s is the free space wavelength of the scattered radiation. If the scattered radiation is the reflected radiation of incident radiation, that is, $\boldsymbol{k}_s = -\boldsymbol{k}_i = -2\pi n_{eff}/\lambda_i \boldsymbol{e}_z$, the momentum conservation condition becomes the first-order Bragg condition Eq. (9.15). The guided light along the core of an optical fibre will be scattered by each FBG plane. If the Bragg condition is not satisfied, the reflected light from each of the subsequent planes becomes progressively out of phase and will eventually cancel out. It will experience very weak reflection at each of the FBG planes because of the

index mismatch. This reflection accumulates over the length of the FBG.

A very important advantage of FBG sensors is that they are wavelength encoded. Shifts in the spectrum, seen as a narrow-band reflection or dip in transmission, are independent of the optical intensity and uniquely associated with each FBG, provided no overlap occurs in each sensor stop-band. FBG sensors have achieved significant applications in monitoring or inspecting the mechanical or temperature response in smart materials and structures. Most of these applications focus on the axial deformation (or strain) and temperature measurements, because the sensitivities to axial deformation and temperature are much higher than those to other modes of deformation.

It is known from Eq. (9.15) that the Bragg wavelength is proportional to the modal index and the FBG spacing period. Both the index and period may change with external conditions which can be divided to temperature and applied disturbances, such as deformations. The induced Bragg wavelength shift of mode j (including polarization mode) can be expressed by:

$$\Delta\lambda_{\mathrm{B}j} = 2\left[\left(n_{\mathrm{eff}\,j}\frac{\partial\Lambda}{\partial T} + \Lambda\frac{\partial n_{\mathrm{eff}\,j}}{\partial T}\right)\Delta T + \sum_i\left(n_{\mathrm{eff}\,j}\frac{\partial\Lambda}{\partial u_i} + \Lambda\frac{\partial n_{\mathrm{eff}\,j}}{\partial u_i}\right)\Delta u_i\right] \quad [9.16]$$

where $n_{\mathrm{eff}\,j}$ and u_i are the effective refractive index of mode j and a perturbation, respectively. Measurement of the perturbation-induced Bragg wavelength shift from a single FBG does not facilitate the discrimination of the response to these variables. The simplest approach is to isolate the unwanted perturbations. In applications, sensors must be embedded with minimal intrusion. In case the deformation sensing is considered, temperature is the main unwanted perturbation. Temperature-compensating methods may be classified as intrinsic or extrinsic. The elimination of cross-sensitivity may be achieved by measurements at two different wavelengths or two different optical modes, in which the strain and the temperature sensitivity are different. The sensor schemes can be constructed by the combination of FBGs with different grating types, such as FBGs with different diameter, different Bragg wavelength, different codope, hybrid FBGs and long period fibre grating, Fabry–Perot cavity, stimulated Brillouin scattering or fibre polarization rocking filter. The measurands may be Bragg wavelength, intensity, Brillouin frequency or polarization rocking resonant wavelength.[54–67] In this chapter, only the optical responses of FBG sensors under deformations are included.

9.3 Optical responses under tension

No significant polarization signals can be observed for FBG sensors under tension. But an FBG sensor has good linear characteristics when it is applied

to measure the axial strain by reflection spectra. According to Eq. (9.16), the relative shift of the Bragg wavelength due to strain is given by:[22]

$$\frac{\Delta\lambda_B}{\lambda_B} = \frac{1}{n_{eff}}\sum_i \frac{\partial n_{eff}}{\partial \xi_i}\xi_i + \frac{1}{\Lambda}\sum_i \frac{\partial \Lambda}{\partial \xi_i}\xi_i \quad [9.17]$$

where ξ_i is the applied strain field to the FBG sensor. According to the photoelastic effect, the first term on the right side of Eq. (9.17) can be written as:

$$\frac{1}{n_{eff}}\sum_i \frac{\partial n_{eff}}{\partial \xi_i}\xi_i = -\frac{n_{eff}^2}{2}\sum_i p_{ij}\xi_i \quad [9.18]$$

where p_{ij} is the strain-optic tensor. For a homogeneous isotropic medium,

$$p_{ij} = \begin{bmatrix} p_{11} & p_{12} & p_{12} & 0 & 0 & 0 \\ p_{12} & p_{11} & p_{12} & 0 & 0 & 0 \\ p_{12} & p_{12} & p_{11} & 0 & 0 & 0 \\ 0 & 0 & 0 & p_{44} & 0 & 0 \\ 0 & 0 & 0 & 0 & p_{44} & 0 \\ 0 & 0 & 0 & 0 & 0 & p_{44} \end{bmatrix} \quad [9.19]$$

where $p_{44} = (p_{11} - p_{12})/2$. For the case of tension, the strain response arises due to both the change in fibre index due to photoelastic effect, and the physical elongation including the corresponding fractional change in grating pitch of the FBG. If a uniaxial longitudinal stress σ_z is applied to the FBG sensor in the z-direction, the resulting strain from first-order elastic theory has three principal components:

$$\xi_i = [-v\xi_z \quad -v\xi_z \quad \xi_z \quad 0 \quad 0 \quad 0]^T \quad [9.20]$$

where the superscript T denotes the transpose of a matrix, $\xi_z = \sigma_z/E$ is the longitudinal strain, E is Young's modulus and v is Poisson's ratio. The index-weighted strain-optic coefficient is then given by:

$$p_{eff} = n_{eff}^2[p_{12} - (p_{11} + p_{12})v]2 \quad [9.21]$$

Hence the right side of Eq. (9.18) can be written as $-p_{eff}\xi_z$.

If it can be assumed that the strain-induced change in the period of the FBG is only dependent on the axial strain, the second term on the right side of Eq. (9.17) will be equal to ξ_z. Equation (9.17) is then expressed as:

$$\Delta\lambda_B/\lambda_B = (1 - p_{eff})\xi_z \quad [9.22]$$

If the fibre is extended at both ends and no body force applied, the fibre core and cladding can be regarded as homogeneous and isotropic, the strain response of the germanosilicate FBG sensor at constant temperature under tension is then given by:

$$(\Delta\lambda_B/\lambda_B)/\xi_z \approx 0.78 \quad [9.23]$$

In a silica fibre there are three transmission wavelength windows in which the losses are very low, such as 0.15 dB/km at 1550 nm. According to Eq. (9.23), typical values for the sensitivity to an applied axial strain in these windows are 1.2 nm/milli-strain at 1550 nm, 1 nm/milli-strain at 1300 nm, and 0.66 nm/milli-strain at 850 nm. The resolutions of FBG are 8.3 micro-strain at 1550 nm, 9.8 micro-strain at 1300 nm and 15 micro-strain at 850 nm by an optical spectrum analyser with a wavelength resolution of 10 pm.

9.4 Optical responses under torsion

Unlike the optical responses of an FBG sensor under tension, the sensitivity of the Bragg wavelength shift of an FBG sensor under torsion is very small. However, the polarization response to torsion is significant. The coupled mode theory can be used to analyse the polarization behaviour of an FBG sensor under torsion.[82]

9.4.1 Shear strain-induced polarization behaviour

The torsion introduces shearing stress in the cross-section of the fibre. If the twisted length of a fibre is L, and the angle of twist is $\phi = \tau L$, where τ is torsion ratio that is the angle of twist per unit length along the axis of the fibre, the matrix for the strain due to this torsion is:

$$\xi_i = [0 \quad 0 \quad 0 \quad \tau x \quad -\tau y \quad 0]^T \quad [9.24]$$

so that the matrix for ΔD_i, perturbation in optical impermeability, is:

$$\Delta D_i = p_{ij}\xi_i = [0 \quad 0 \quad 0 \quad p_{44}\tau x \quad -p_{44}\tau y \quad 0]^T \quad [9.25]$$

The relationship between the dielectric permittivity perturbation and the optical impermeability perturbation can be expressed as:

$$\tilde{\varepsilon}_{\text{torsion } ij} = -n_{co}^4 \Delta D_{ij} \quad [9.26]$$

The induced polarization behaviour can be analysed by using Eq. (9.26) and Subsection 9.2.2. The induced circular birefringence in a single mode optical fibre is given by:[83]

$$B_c = n_{co}\tau\lambda(p_{11} - p_{12})/(2\pi) \quad [9.27]$$

9.4.2 UV-induced polarization behaviour

The polarization of pulse UV beam and asymmetric geometry associated with the side-exposure of UV light during the FBG fabrication process[84,85] will

induce linear birefringence. The peak birefringence of the FBG can be calculated from the expression:[84]

$$\Delta n = \frac{\lambda}{2\pi \cdot L} |\,\text{phase}(Q_1) - \text{phase}(Q_2)| \qquad [9.28]$$

where L is the length of the FBG, Q_1 and Q_2 are the eigenvalues of the corresponding Jones matrix:

$$\det[T(t)T^{-1}(0) - QI] = 0 \qquad [9.29]$$

where $\boldsymbol{T}$, t and I are the Jones matrix, the time from the beginning of the UV exposure and the identity matrix, respectively. The symbol det and the superscript $^{-1}$ denote the determinant and the inverse of a matrix, respectively. Based on the birefringence, a permittivity perturbation tensor can be used to represent its polarization behaviour:

$$\tilde{\varepsilon}_{\text{UV}} = \begin{bmatrix} \Delta\varepsilon_x & 0 & 0 \\ 0 & \Delta\varepsilon_y & 0 \\ 0 & 0 & 0 \end{bmatrix} \qquad [9.30]$$

where $\Delta\varepsilon_y - \Delta\varepsilon_x = 2n_{\text{eff}} \cdot \Delta n$. By considering the azimuth ϕ of the faster or slow axis of the FBG sensor and the tilted angle ϑ, Eq. (9.30) becomes:

$$\tilde{\varepsilon}'_{\text{UV}} = \boldsymbol{T}_z \boldsymbol{T}_x \tilde{\varepsilon}_{\text{UV}} \boldsymbol{T}_x^T \boldsymbol{T}_z^T \qquad [9.31]$$

where $\boldsymbol{T}_z$ and $\boldsymbol{T}_x$ are the rotation matrix around z, x axes, respectively. The induced polarization behaviour can be analysed by using Eq. (9.31) and Subsection 9.2.2.

In the case of an FBG sensor under torsion, both shear strain-induced birefringence and UV-induced birefringence are considered:

$$\tilde{\varepsilon}_{ij} = \tilde{\varepsilon}_{\text{torsion } ij} + \tilde{\varepsilon}'_{\text{UV}} \qquad [9.32]$$

There are UV-induced linear birefringence and shear strain-induced circular birefringence in the fibre.

9.4.3 Simulated and experimental results

In numeric simulations, the parameters of the FBG sensor are the same as those used in the corresponding experiments. The core radius, cladding radius and the effective refractive index are 4.25 μm, 62.5 μm and 1.46, respectively. The strain-optic coefficients p_{11} and p_{12} are taken as 0.113 and 0.252, respectively.

Based on the preceding theoretical analysis, the FBG sensors can be treated as the wave-plates. Apparently, when an FBG sensor is under torsion, these

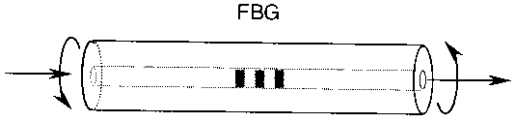

9.2 FBGs under torsion. The length of the FBG and the torsion gauge of the fibre are 1 cm and 17.5 cm, respectively.

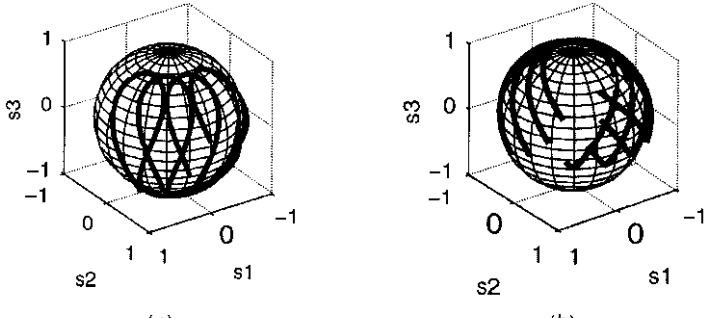

9.3 Simulated polarization signals of an FBG under torsion. The orientation is 0, $\pi/12$, $\pi/6$, $\pi/4$, respectively, and the angle of ellipticity is zero in (*a*), and $\pi/8$ in (*b*).

wave-plates will be rotated. This means the geometric parameter, the azimuth ϕ, will be changed during the twisting of an optical fibre. Then the output polarization signals will represent the combination effects of the torsion-induced circulation birefringence and the UV irradiation-induced linear birefringence.

The torsion model under investigation is shown in Fig. 9.2, where the FBG is located at the middle point of an optical fibre. The experimental setup is similar to that of T. Erdogan and V. Mizrahi,[84] and the UV-induced birefringence of a FBG is approximately 2.5×10^{-5}. The wavelength of the incident laser is set at 1525 nm, and the loading rotation angle is from 0 to 360°. The simulated results are presented in Fig. 9.3. According to these simulations, the initial orientations do not appear to affect the shape of the output polarization signals. However, the ellipticity of the input light will affect the output polarization signals significantly.

The position of the FBG can influence the output polarization signals significantly. On one side, it will change the direction of the angular velocity vector of the FBG sensor, and on the other side, it will provide a different initial state of polarization from the FBG segment. Although both their directions vary along the equator in a generalized Poincaré sphere, their respective variation velocities are different. These differences will result in different output polarization signals for various FBG sensor positions.

Figure 9.4 shows one measured polarization signal of an FBG sensor under

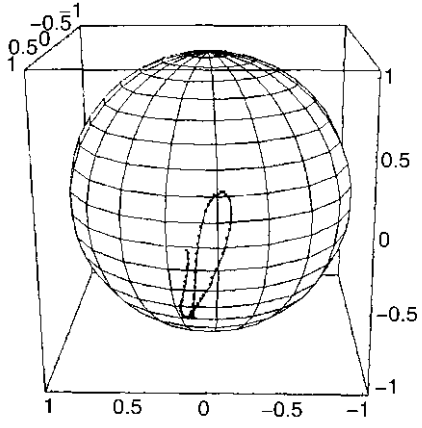

9.4 Measured polarization signal of an FBG under torsion.

torsion. The twisted length was 17.5 cm, the Bragg wavelength without external strain was 1555 nm, the wavelength of incident laser was 1525 nm, the torsion ratios were 0–0.36 rad/cm with a step of 0.005 rad/cm. The states of polarization were measured by a commercial polarimeter. The simulated result coincides with the experimental result.

The reflective spectrum of the FBG sensor was measured by an optical spectrum measuring system composed of a tunable laser, an optical power meter with GP-IB interface, and a computer. The wavelength resolution is 10 pm. The measured wavelength shift under the torsion ratio of 1 rad/cm is smaller than the resolution of the optical spectrum measuring system.

9.5 Optical responses under lateral compression

In the case of optical fibres under lateral compression, linear birefringence will be induced based on the strain–optic relationship. Thus a fibre can be used to sense the lateral compression by measuring the change of state of polarization of travelled light. For general FBG sensors the wavelength-compression sensitivity is relatively small compared with the axial strain sensitivity, but spectrum bifurcation, or spectrum split, will occur with the compression-induced birefringence in optical fibres.[86] The transverse strain can also be sensed by an FBG written into a polarization-maintaining fibre (PMF) by measuring the Bragg wavelength shifts of two reflective peaks associated with the orthogonal polarization modes.[87–95] In addition, transverse strain can be measured by a long-period fibre grating.[96]

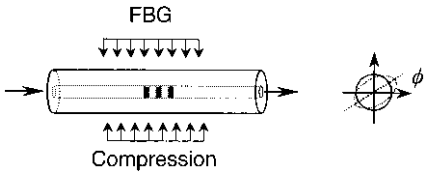

9.5 FBG under lateral compression. The length of FBG and compressed length of fibre are 1 cm and 1.8 cm, respectively.

9.5.1 Polarization responses under lateral compression

The strain of an optical fibre under lateral compression will induce linear birefringence. Since the glass optical fibre is a rigid medium, the birefringence induced by the geometric property, such as tilted angle for tilted FBG, is small. The polarization behaviour of the FBG under lateral compression can be determined by the combination effects of both the compression-induced linear birefringence and the UV-induced linear birefringence.

The case that an uncoated silica optical fibre is laminated by two rigid plates is considered, as shown in Fig. 9.5. Since the silica optical fibre is a rigid medium, this contact problem can be simplified to line force loading. Then the close form of the stress solutions can be obtained with the help of the plane stress assumption. Since the electric field in a single mode fibre is concentrated in the core region, the solution in the centre is approximately selected to represent the stress of a single mode fibre under lateral compression. The stress in the core can be expressed as:

$$\sigma_{11} = f/(\pi \cdot r_{cl}) \quad [9.33]$$

$$\sigma_{22} = -3f/(\pi \cdot r_{cl}) \quad [9.34]$$

$$\sigma_{33} = 0 \quad [9.35]$$

$$\tau_{12} = \tau_{23} = \tau_{31} = 0 \quad [9.36]$$

where f is the lateral loading, and r_{cl} is the radius of optical fibre cladding. Based on the strain–optic relationship, the permittivity perturbation $\tilde{\varepsilon}_{ij}$ can be derived. It can be inserted into the coupled mode equations, Eqs. (9.4) and (9.5), and the coupled mode coefficients can be obtained by coupling integrals, Eq. (9.6). The strain induces a linear birefringence:

$$B_1 = \left(\frac{4n_{co}^3 \cdot f}{\lambda E \cdot r_0}\right)(1 + v)(p_{12} - p_{11}) \quad [9.37]$$

In the simulated analysis, the lateral loading is from 0 to 1000 N/m, and the

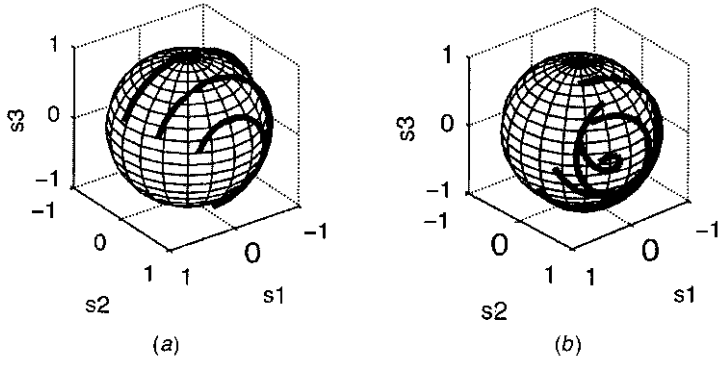

9.6 Polarization signals of FBG under lateral compression. The normal compression is shown in (*a*), and slant compression with 45° in (*b*); the angle of ellipticity is 0. The orientations are 0, $\pi/12$, $\pi 6$ and $\pi/4$, respectively.

permittivity perturbation $\tilde{\varepsilon}_{ij}$ induced by the transverse strain and UV-induced birefringence are considered together. For a normal lateral compression, the UV irradiation-induced birefringence axis coincides with the strain-induced birefringence. Since the silica optical fibre is a rigid medium, the compression-induced displacement is small, and it has little effect on the geometric parameters of the UV-induced perturbation. Thus, the output polarization signal is the same as the single mode fibre. The output polarization signals are shown in Fig. 9.6(*a*). They are insensitive to the FBG position.

For a slant compression, there is an angle between the strain- and UV irradiation-induced birefringence axis. Though the UV irradiation-induced component change is small during the loading, it still affects the output polarization signals during the compression. Apparently, the effects are related to the angle and the position of the FBG. The output polarization signals are shown in Fig. 9.6(*b*).

9.5.2 Spectrum responses under lateral compression

As shown in the previous section, lateral compression will induce linear birefringence in a single mode optical fibre. This means that a difference of the propagation constants in the two orthogonal polarization modes in the fibre is induced. Based on the phase-matching condition Eq. (9.15), these two propagation constants correspond to two different Bragg wavelengths. Thus, with the increasing of compression loading, the spectrum bifurcation or spectrum split will be observed. An extended multidimension measurement is applying the double wavelength measurement in the birefringent FBG. Since the effective indices of the orthogonal LP modes are different from each other

in birefringent optical fibre, every FBG in a birefringent fibre has two corresponding Bragg wavelengths. If we write two different FBGs in a single optical fibre, then it is expected to obtain four different Bragg wavelengths, which can establish four equations as Eq. (9.16), and to measure not only the axial strain and temperature, but also two transverse strain components.

In the case of lateral compression, the propagated fundamental mode HE_{11} perfectly degenerates into x- and y-polarized modes with different propagation constants. According to the photoelastic effect and the stress–strain relationship, the effective index changes of the two polarized modes can be expressed as:[86]

$$\Delta n_{\mathrm{eff}x}(x,y,z) = -\frac{n_{\mathrm{eff}}^3}{2E}\{(p_{11}-2vp_{12})\sigma_x(x,y,z) + [(1-v)p_{12}-vp_{11}]\sigma_y(x,y,z)\} \quad [9.38]$$

$$\Delta n_{\mathrm{eff}y}(x,y,z) = -\frac{n_{\mathrm{eff}}^3}{2E}\{(p_{11}-2vp_{12})\sigma_y(x,y,z) + [(1-v)p_{12}-vp_{11}]\sigma_x(x,y,z)\} \quad [9.39]$$

Using the stress–strain relationship and Eq. (9.17), the relative shifts of the Bragg wavelength of two polarized modes at any point of the FBG due to lateral compression are then obtained by:

$$\frac{\Delta\lambda_{\mathrm{B}x}}{\lambda_{\mathrm{B}}} = -\frac{n_{\mathrm{eff}}^2}{2E}\{(p_{11}-2vp_{12})\sigma_x(x,y,z) + [(1-v)p_{12}-vp_{11}]\sigma_y(x,y,z)\} - v[\sigma_x(x,y,z)+\sigma_y(x,y,z)]/E \quad [9.40]$$

$$\frac{\Delta\lambda_{\mathrm{B}y}}{\lambda_{\mathrm{B}}} = -\frac{n_{\mathrm{eff}}^2}{2E}\{(p_{11}-2vp_{12})\sigma_y(x,y,z) + [(1-v)p_{12}-vp_{11}]\sigma_x(x,y,z)\} - v[\sigma_x(x,y,z)+\sigma_y(x,y,z)]/E \quad [9.41]$$

The spectrum split of the polarized modes at any point is then given by:

$$\frac{\Delta\lambda_{\mathrm{B}y}(x,y,z)-\Delta\lambda_{\mathrm{B}x}(x,y,z)}{\lambda_{\mathrm{B}}} = -\frac{n_{\mathrm{eff}}^2}{2E}(1+v)(p_{11}-p_{12})[\sigma_y(x,y,z) - \sigma_x(x,y,z)] \quad [9.42]$$

Figure 9.7 represents the reflection spectra of an FBG under different lateral loads. The spectrum of the FBG splits in more than one peak at the Bragg wavelength. For higher values of applied force, the peaks become totally separate.

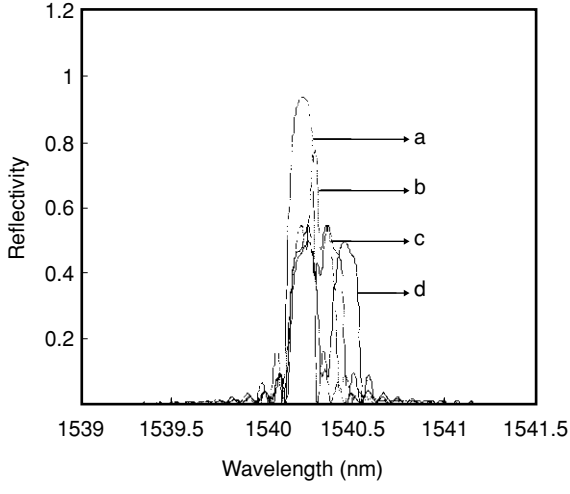

9.7 Reflection spectra of an FBG sensor under lateral compression (loadings a–d are 0.0, 1.5, 2.0 and 3.0 kN/m, respectively), the angle between the orientation of input linear polarized light and the compression direction is 45°.

9.6 Optical responses under bending

The major effects of FBG under bending (see Fig. 9.8) may come from the geometrically bent structure and non-uniform lateral stress. Using the perturbation method, the scalar propagation characteristics of a geometrically bent optical waveguide can be analysed. Corrected electric fields or Gaussian approximations have been proposed to describe the field deformations.[97,98] The equivalent straight waveguide is often used to describe its electric field in the bent waveguide. More rigorous description adopted a full-vectorial wave propagation theory.[99] Based on the photoelastic relationship, the non-uniform stress distribution-induced birefringence has been presented.[100–102] The induced linear birefringence can be expressed as:[83]

$$B_1 = 0.25 n_{co}^2 (p_{11} - p_{12})(1 + v)(r_{cl}/r_{bent})^2 \qquad [9.43]$$

Assuming that the mode holds and the phase-matching condition works well in the bent FBG, the effects under bending can be qualitatively analysed. Then the shift of Bragg wavelength is determined by the changes of propagation constants or effective refractive index, and grating period. In the case of stress-induced birefringence, only the effects of non-uniform lateral compressive stress are considered, since it is only sensitive to the difference of that in two orthogonal directions. But, in order to obtain an absolute change of refractive index, the effect of the axis component is required. According to the

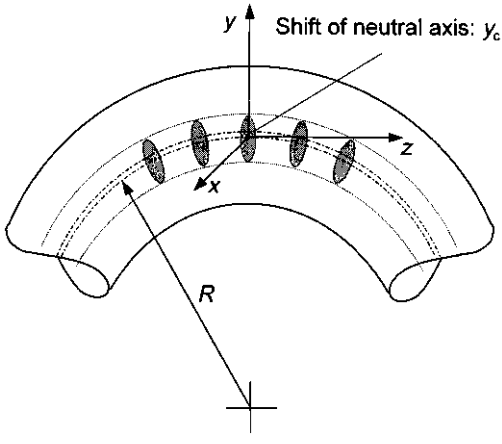

9.8 Fibre Bragg gratings under bending.

photoelastic relationship, the index of the optical fibre is decreased by tension and is increased by compression. Since the electric field in the bent optical fibre shifts towards the outer core/cladding boundary, and the outer side of the bent optical fibre is under tension, the field deformation will induce a decrement of effective refractive index. Apparently due to the birefringence of the bending optical fibre, two independent Bragg wavelengths occur. The difference of these two Bragg wavelengths is small, and only a broader bandwidth of reflection spectrum can be observed.[103]

Another characteristic of the silica fibre is the non-linear stress–strain relationship. It is known that the neutral axis is also shifted toward the outer side of the fibre under bending.[104] Its direct effect on the FBG is that the grating period will be compressed, so these effects should also be considered, together with the change of effective refractive index of the FBG under bending.

Other fibre gratings can also be used in bend sensing, such as long-period fibre grating[105,106] and multicore fibre Bragg gratings.[107]

9.7 Conclusions

This chapter has given the optical responses of FBG sensors under different modes of deformation. Both the polarization behaviour and optical spectrum of FBGs have been used to analyse the deformation perturbations. In the case of an FBG under tension, the wavelength sensitivity to tension is significant. In the case of torsion, the wavelength sensitivity is very small, and the polarization behaviour is sensitive to it. In the case of lateral compression, the wavelength sensitivity is much smaller than that under tension, but the deformation induced birefringence can broaden and split the reflection peaks.

Table 9.1 Optical responses of normal germanosilicate FBG under different deformations

Mode of deformation	Optical response		
	Bragg wavelength shift [14,85,102]	UV induced linear birefringence[83] B_l	Deformation induced linear/circular birefringence[82,85] B_l/B_c
Tension	1200 pm/m ε, at wavelength 1550 nm	2.5×10^{-5}	0
Torsion	< 10 pm, at torsion ratio 0.072 rad/mm, from experiment	2.5×10^{-5}	$B_l = 9.7 \times 10^{-7}\ \tau$, $[\tau]$ = rad/mm, at wavelength 1550 nm
Lateral compression	2.0 pm/N (parallel), 8.6 pm/N (perpendicular), with compression length 10 mm	2.5×10^{-5}	$B_l = 5.1 \times 10^{-4}$, at 10 N/mm
Pure bending	< 260 pm, at curvature 2.43 cm^{-1}	2.5×10^{-5}	$B_l = 1.5 \times 10^{-5}\ (1/r_{bent})^2$, $[r_{bent}]$ = cm

The lateral compression can be sensed by the spectrum behaviour in some sensing schemes. Both the polarization behaviour and the optical spectrum of FBGs can be used to analyse lateral compression. Bending of FBGs can be analysed for both the polarization behaviour and the optical spectrum, but it is difficult to measure the polarization evolution of fibre under bending. The optical responses of normal germanosilicate FBG under different individual modes of deformations are summarized in Table 9.1.

In practical FBG sensors, temperature must be considered in the spectrum because of their high sensitivity to temperature. Some approaches include isolating or compensating or simultaneously measuring the temperature perturbation.

Acknowledgements

The authors wish to thank Hong Kong Research Grants Council for supporting this work (Grant No. PolyU5112/98E).

References

1 Gardner J W, *Microsensors*: *Principles and Applications*, John Wiley & Sons, Chichester, UK, 1994.
2 Yang X and Young R J, 'Determination of residual strains in ceramic-fibre

reinforced composites using fluorescence spectroscopy', *Acta Metallurgica et Materialia*, 1995, **43**(6), 2407–16.
3 Grattan K T V and Sun T, 'Fiber optic sensor technology: an overview', *Sensors and Actuators*, A-Physical, 2000, **82**(1–3), 40–61.
4 Posey R and Vohra S T, 'An eight-channel fiber-optic Bragg grating and stimulated Brillouin sensor system for simultaneous temperature and strain measurements', *IEEE Photonics Technol. Lett*., 1999, **11**(12), 1641–3.
5 Brown A W, DeMerchant M D, Bao X et al., 'Spatial resolution enhancement of a Brillouin-distributed sensor using a novel signal processing method', *IEEE J. Lightwave Technol*., 1999, **17**(7), 1179–83.
6 Kim S H, Lee J J, Lee D C et al., 'A study on the development of transmission-type extrinsic Fabry–Perot interferometric optical fiber sensor', *IEEE J. Lightwave Technol*., 1999, **17**(10), 1869–74.
7 Udd E, *Fiber Optic Sensors*: *An Introduction for Engineers and Scientists*, John Wiley & Sons, New York, 1991.
8 Van Steenkiste R J, *Strain and Temperature Measurement with Fiber Optic Sensors*, Technomic Publishing Company, Lancaster, 1997.
9 Johnson P, 'Strain field measurements with dual-beam digital speckle photography', *Optics Lasers Eng*., 1998, **30**(3–4), 315–26.
10 Johnson P, 'Strain field measurements in industrial applications using dual-beam digital speckle photography', *Optics Lasers Eng*., 1998, **30**(5), 421–31.
11 Hack E and Broennimann R, 'Electronic speckle pattern interferometry deformation measurement on lightweight structures under thermal load', *Optics Lasers Eng*., 1999, **31**(3), 213–22.
12 Rae P J, Goldrein H T, Bourne N K et al., 'Measurement of dynamic large-strain deformation maps using an automated fine grid technique', *Optics Lasers Eng*., 1999, **31**(2), 113–22.
13 Kersey A D, Davis M A, Patrick H J et al., 'Fiber grating sensors', *IEEE J. Lightwave Technol*., 1997, **15**(8), 1442–63.
14 Othonos A and Kalli K, *Fiber Bragg Gratings*: *Fundamentals and Applications in Telecommunications and Sensing*, Artech House, Boston, 1999.
15 Rao Y J, 'In-fiber Bragg grating sensors', *Measurement Sci. Technol*., 1997, **8**(4), 355–75.
16 Rao Y J, 'Recent progress in applications of in-fiber Bragg grating sensors', *Optics Lasers Eng*., 1999, **31**(4), 297–324.
17 Friebele E J, 'Fiber Bragg grating strain sensors: present and future applications in smart structures', *Optics Photon. News*, 1999, **9**(1), 33–7.
18 Hill K O and Meltz G, 'Fiber Bragg grating technology fundamentals and overview', *IEEE J. Lightwave Technol*., 1997, **15**(8), 1263–76.
19 Kashyap R, *Fiber Bragg Gratings*, Academic Press, San Diego, 1999.
20 Meltz G, 'Overview of fiber grating-based sensors'. In *Proc. SPIE–Distributed and Multiplexed Fiber Optic Sensors VI*, 1996, **2838**, 2–22.
21 Goyal A and Muendel M, 'Optical fiber Bragg gratings have a wide variety of uses', *Photonics Spectra*, 1998, **32**(9), 116–22.
22 Udd E, *Fiber Optic Smart Structures*, John Wiley, New York, 1995.
23 Morey W W, Ball G A and Singh H, 'Applications of fiber Bragg grating sensors'. In *Proc. SPIE – Fiber Optic and Laser Sensors XIV*, 1996, **2839**, 2–7.

24 Measures R M, Maaskant R, Alavie T et al., 'Fiber-optic Bragg gratings for bridge monitoring', *Cement Concrete Composites*, 1997, **9**(1), 21–3.
25 Meissner J, Nowak W, Slowik V et al., 'Strain monitoring at a prestressed concrete bridge'. In *Proc. 12th Int. Conf. Optical Fiber Sensors*, Williamsburg, 48–51, 1997.
26 Schulz W L, Udd E, Seim J M et al., 'Advanced fiber grating strain sensor systems for bridges, structures, and highways'. In *Proc. SPIE – Smart Structures and Materials 1998: Smart Systems for Bridges, Structures, and Highways*, 1998, **3325**, 212–21.
27 Prohaska J D, Snitzer E, Chen B et al., 'Fiber optic Bragg grating strain sensor in large scale concrete structures'. In *Proc. SPIE – Fiber Optic Smart Structures and Skins V*, 1992, **1798**, 286–94.
28 Du W C, Tao X M, Tam H Y et al., 'Fundamentals and applications of optical fiber Bragg grating sensors to textile structural composites', *Composite Structures*, 1998, **42**(3), 217–29.
29 Jin X D, Sirkis J S, Venkateswaran V S et al., 'Simultaneous measurement of two strain components in composite structures using embedded fiber sensors'. In *Proc. 12th Int. Conf. Optical Fiber Sensors*, Williamsburg, 44–7, 1997.
30 Ferdinand P, Ferragu O, Lechien J L et al., 'Mine operating accurate stability control with optical fiber sensing and Bragg grating technology: the European BRITE/EURAM STABILOS project', *IEEE J. Lightwave Technol.*, 1995, **13**(7), 1303–13.
31 Hjelme D R, Bjerkan L, Neegard S et al., 'Application of Bragg grating sensors in the characterization of scaled marine vehicle modes', *Appl. Optics*, 1997, **36**(1), 328–36.
32 Friebele E J, Askins C G, Bosse A B et al., 'Optical fiber sensors for spacecraft applications', *Smart Mater. Struct.*, 1999, **8**(6), 813–38.
33 Ezbiri A, Kanellopoulos S E and Handerek V A, 'High resolution instrumentation system for demodulation of Bragg grating aerospace sensors', In *Proc. 12th Int. Conf. Optical Fiber Sensors*, Williamsburg, 456–9, 1997.
34 Tang L Q, Tao X M and Choy C L, 'Effectiveness and optimization of fiber Bragg grating sensor as embedded strain sensor', *Smart Mater. Struct.*, 1999, **8**(1), 154–60.
35 Rao Y J, Webb D J, Jackson D A et al., 'In-fiber Bragg grating temperature sensor system for medical applications', *IEEE J. Lightwave Technol.*, 1997, **15**(5), 779–85.
36 Arie A, Lissak B and Tur M, 'Static fiber-Bragg grating strain sensing using frequency-locked lasers', *IEEE J. Lightwave Technol.*, 1999, **17**(10), 1849–55.
37 Kersey A D, Berkoff T A and Morey W W, 'Multiplexed fiber Bragg grating sensor system with a fiber Fabry–Perot wavelength filter', *Optics Lett.*, 1993, **18**(16), 1370–2.
38 Davis M A, Bellemore D G and Kersey A D, 'Design and performance of a fiber Bragg grating distributed strain sensor system'. In *Proc. SPIE – Smart Structures and Materials 1995: Smart Systems for Bridges, Structures, and Highways*, 1995, **2446**, 227–35.
39 Kersey A D, Davis M A and Bellemore D G, 'Development of fiber sensors for structural monitoring'. In *Proc. SPIE – Nondestructive Evaluation of Aging Bridges and Highways*, 1995, **2456**, 262–8.
40 Dunphy J R, Ball G, Amato F D et al., 'Instrumentation development in support of fiber grating sensor arrays', In *Proc. SPIE – Distributed and Multiplexed Fiber Optic Sensors III*, 1993, **2071**, 2–11.

41 Jackson D A, Ribeiro A B L, Reekie L et al., 'Simple multiplexing scheme for a fiber optic grating sensor network', *Optics Lett*., 1993, **18**(14), 1192–4.
42 Davis M A and Kersey A D, 'A fiber Fourier transform spectrometer for decoding fiber Bragg sensors', *IEEE J. Lightwave Technol*., 1995, **13**(7), 1289–95.
43 Kersey A D and Berkoff T A, 'Fiber optic Bragg differential temperature sensor', *IEEE Photon. Technol. Lett*., 1992, **4**(10), 1183–5.
44 Ferreira L A, Diatzikis E V, Santos J L et al., 'Frequency-modulated multimode laser diode for fiber Bragg grating sensors', *IEEE J. Lightwave Technol*., 1998, **16**(9), 1620–30.
45 Moreira P J, Ferreira L A, Santos J L et al., 'Dynamic range enhancement in fiber Bragg grating sensors using a multimode laser diode', *IEEE Photon. Technol. Lett*., 1999, **11**(6), 703–5.
46 Tanaka Y and Ogusu K, 'Tensile-strain coefficient of resonance frequency of depolarized guided acoustic-wave Brillouin scattering', *IEEE Photonics Technol. Lett*., 1999, **11**(7), 865–7.
47 Lissak B, Arie A and Tur M, 'Highly sensitive dynamic strain measurements by locking lasers to fiber Bragg gratings', *Optics Lett*., 1998, **23**(24), 1930–2.
48 Ogawa O, Kato T and Kamikatano M, 'Technique for measuring the dynamic strain on an optical fiber based on Brillouin ring amplification', *IEEE J. Lightwave Technol*., 1999, **17**(2), 234–42.
49 McGarrity C and Jackson D A, 'A network for large numbers of interferometric sensors and fiber Bragg gratings with high resolution and extended range', *IEEE J. Lightwave Technol*., 1998, **16**(1), 54–65.
50 Berkoff T A, Davis M A, Bellemore D G et al., 'Hybrid time and wavelength division multiplexed fiber grating array', In *Proc. SPIE – Smart Structures and Materials 1995: Smart Sensing, Processing, and Instrumentation*, 1995, **2444**, 288–94.
51 Friebele E J, Putnam M A, Patrick H J et al., 'Ultrahigh-sensitivity fiber-optic strain and temperature sensor', *Optics Lett*., 1998, **23**(3), 222–4.
52 Chan C C, Jin W, Rad A B et al., 'Simultaneous measurement of temperature and strain: an artificial neural network approach', *IEEE Photon. Technol. Lett*., 1998, **10**(6), 854–6.
53 James S W, Dockney M L and Tatam R P, 'Simultaneous independent temperature and strain measurement using in-fiber Bragg grating sensors', *Electron. Lett*., 1996, **32**(12), 1133–4.
54 Xu M G, Archambault J L, Reekie L et al., 'Discrimination between strain and temperature effects using dual-wavelength fiber grating sensors', *Electron. Lett*., 1994, **30**(13), 1085–7.
55 Cavaleiro P M, Araújo F M, Ferreira L A et al., 'Simultaneous measurement of strain and temperature using Bragg gratings written in germanosilicate and boron-codoped germanosilicate fibers', *IEEE Photon. Technol. Lett*., 1999, **11**(12), 1635–7.
56 Patrick H J, Williams G M, Kersey A D et al., 'Hybrid fiber Bragg grating/long period fiber grating sensor for strain/temperature discrimination', *IEEE Photon. Technol. Lett*., 1996, **8**(9), 1223–5.
57 Du W C, Tao X M and Tam H Y, 'Temperature independent strain measurement with a fiber grating tapered cavity sensor', *IEEE Photon. Technol. Lett*., 1999, **11**(5), 596–8.

58 Du W C, Tao X M and Tam H Y, 'Fiber Bragg grating cavity sensor for simultaneous measurement of strain and temperature', *IEEE Photon. Technol. Lett*., 1999, **11**(1), 105–7.
59 Lo Y L, 'In-fiber Bragg grating sensors using interferometric interrogations for passive quadrature signal processing', *IEEE Photon. Technol. Lett*., 1998, **10**(7), 1003–5.
60 Koo K P, LeBlanc M, Tsai T E et al., 'Fiber-chirped grating Fabry–Perot sensor with multiple-wavelength-addressable free-spectral ranges', *IEEE Photon. Technol. Lett*., 1998, **10**(7), 1006–8.
61 Smith J, Brown A, DeMerchant M et al., 'Simultaneous strain and temperature measurement using a Brillouin scattering based distributed sensor'. In *Proc. SPIE – Smart Structures and Materials 1999: Sensory Phenomena and Measurement Instrumentation for Smart Structures and Materials*, 1999, **3670**, 366–73.
62 Kanellopoulos S E, Handerek V A and Rogers A, 'Simultaneous strain and temperature sensing with photogenerated in-fiber gratings', *Optics Lett*., 1995, **20**(3), 333–5.
63 Kang S C, Kim S Y, Lee S B et al., 'Temperature-independent strain system using a tilted fiber Bragg grating demodulator', *IEEE Photon. Technol. Lett*., 1998, **10**(10), 1461–3.
64 Sinha P G and Yoshino T, 'Acoustically scanned low-coherence interrogated simultaneous measurement of absolute strain and temperature using highly birefringent fibers', *IEEE J. Lightwave Technol*., 1998, **16**(11), 2010–15.
65 Yun S H, Richardson D J and Kim B Y, 'Interrogation of fiber grating sensor arrays with a wavelength-swept fiber laser', *Optics Lett*., 1998, **23**(11), 843–5.
66 Putnam M A, Dennis M L, Duling III I N et al., 'Broadband square-pulse operation of a passively mode-locked fiber laser for fiber Bragg grating interrogation', *Optics Lett*., 1998, **23**(2), 138–40.
67 LeBlanc M, Huang S, Ohn M et al., 'Distributed strain measurement based on a fiber Bragg grating and its reflection spectrum analysis', *Optics Lett*., 1996, **21**(17), 1405–7.
68 Huang S, Ohn M M and Measures R M, 'A novel Bragg grating distributed-strain sensor based on phase measurements'. In *Proc. SPIE – Smart Structures and Materials 1995: Smart Sensing, Processing, and Instrumentation*, 1995, **2444**, 158–69.
69 Volanthen M, Geiger H and Dakin J P, 'Distributed grating sensors using low-coherence reflectometry', *IEEE J. Lightwave Technol*., 1997, **15**(11), 2076–82.
70 Bhatia V and Vengsarkar A M, 'Optical fiber long-period grating sensors', *Optics Lett*., 1996, **21**(9), 692–4.
71 Patrick H, Kersey A D, Pedrazzani J R et al., 'Fiber Bragg grating demodulation system using in-fiber long period grating filters'. In *Proc. SPIE – Distributed and Multiplexed Fiber Optic Sensors VI*, 1996, **2838**, 60–5.
72 Kersey A D and Morey W W, 'Multiplexed Bragg grating fiber laser strain sensor system with mode-locked interrogation', *Electron. Lett*., 1993, **29**(1), 112–14.
73 Kersey A D and Morey W W, 'Multi-element Bragg grating based fiber laser strain sensor', *Electron. Lett*., 1993, **29**(11), 964–66.
74 Koo K P and Kersey A D, 'Bragg grating based laser sensor systems with interferometric interrogation and wavelength division multiplexing', *IEEE J. Lightwave Technol*., 1995, **13**(7), 1243–9.

75 Born M and Wolf E, *Principles of Optics*, 7th (Expanded) edn, Cambridge University Press, Cambridge, 1999.
76 Huard S, *Polarization of Light*, John Wiley, New York, 1997.
77 Ulrich R and Simon A, 'Polarisation optics of twisted single-mode fibers', *Appl. Optics*, 1979, **18**(13), 2241–51.
78 Buck J A, *Fundamentals of Optical Fibers*, John Wiley, New York, 1995.
79 Zhou W, Chen X F and Yang D X, *Fundamentals of Photonics*, Zhejiang University Press, Hangzhou, 2000.
80 Marcuse D, *Theory of Dielectric Optical Waveguides*, 2nd edn, Academic Press, Boston, 1991.
81 Wangsness R K, *Electromagnetic Fields*, John Wiley, New York, 1979.
82 Zhang A P, Tao X M and Tam H Y, Prediction of polarization behavior of twisted optical fibres containing Bragg grating sensors, *J. Textile Inst*., 2000, Part 3, 105–16.
83 Jeunhomme L B, *Single-Mode Fiber Optics*: *Principles and Applications*, 2nd edn, Marcel Dekker, New York, 1990.
84 Erdogan T and Mizrahi V, 'Characterization of UV-induced birefringence in photosensitive Ge-doped silica optical fiber', *J. Opt. Soc. Amer. B*, 1994, **11**(10), 2100–5.
85 Vengarkar A M, Zhong Q, Inniss D et al., 'Birefringence reduction in side-written photoinduced fiber devices by a dual-exposure method', *Optics Lett*., 1994, **19**(16), 1260–2.
86 Gafsi R and El-Sherif M A, 'Analysis of induced-birefringence effects on fiber Bragg gratings', *Opt. Fiber Technol*., 2000, **6**(3), 299–323.
87 Kawase L R, Valente L C G, Margulis W et al., 'Force measurement using induced birefringence on Bragg grating'. In *Proc. 1997 SBMO/MTT-S International Microwave and Optoelectronics Conference*, (1) 394–6, 1997.
88 Lawrence C M, Nelson D V, Makino A et al., 'Modeling of the multi-parameter Bragg grating sensor', In *Proc. SPIE – Third Pacific Northwest Fiber Optic Sensor Workshop*, 1997, **3180**, 42–9.
89 Udd E, Nelson D V and Lawrence C M, 'Multiple axis strain sensing using fiber gratings written onto birefringent single mode optical fiber', In *Proc. 12th Int. Conf. Optical Fiber Sensors*, Williamsburg, 48–51, 1997.
90 Udd E, Lawrence C M and Nelson D V, 'Development of a three axis strain and temperature fiber optical grating sensor'. In *Proc. SPIE – Smart Structures and Materials* 1997: *Smart Sensing, Processing, and Instrumentation*, 1997, **3042**, 229–36.
91 Udd E, Schulz W L, Seim J M et al., 'Transverse fiber grating strain sensors based on dual overlaid fiber gratings on polarization preserving fibers'. In *Proc. SPIE – Smart Structures and Materials 1998: Sensory Phenomena and Measurement Instrumentation for Smart Structures and Materials*, 1998, **3330**, 253–63.
92 Udd E, Schulz W L and Seim J M, 'Measurement of multidimensional strain fields using fiber grating sensors for structural monitoring'. In *Proc. SPIE – Fiber Optic Sensor Technology and Applications*, 1999, **3860**, 24–34.
93 Udd E, Schulz W L and Seim J M, 'Multi-axis fiber grating strain sensor applications for structural monitoring and process control'. In *Proc. SPIE – Process Monitoring Applications of Fiber Optic Sensors*, 1999, **3538**, 206–14.
94 LeBlanc M, Vohra S T, Tsai T E et al., 'Transverse load sensing by use of pi-phase-shifted fiber Bragg gratings', *Optics Lett*., 1999, **24**(16), 1091–3.

95 Canning J and Sceats M G, 'π-phase-shifted periodic distributed structures in optical fibers by UV post-processing', *Electron. Lett*., 1994, **30**(16), 1344–5.
96 Liu Y, Zhang L, Bennion I, 'Fibre optic load sensors with high transverse strain sensitivity based on long-period gratings in B/Ge co-doped fibre', *Electron. Lett*., 1999, **35**(8), 661–3.
97 Gambling W A, Matsumura H and Ragdale C M, 'Field deformation in a curved single-mode fiber', *Electronics Lett*., 1978, **14**(5), 130–2.
98 Garth S J, 'Modes on a bent optical wave-guide', *IEE Proc. J*: *Optoelectronics*, 1987, **134**(4), 221–9.
99 Lui W W, Xu C L, Hirono T et al., 'Full-vectorial wave propagation in semiconductor optical bending waveguides and equivalent straight waveguide approximations', *J. Lightwave Technol*., 1998, **16**(5), 910–14.
100 Ulrich R, Rashleigh S C and Eichoff W, 'Bending-induced birefringence in single mode fibers', *Optics Lett*., 1980, **5**(6), 273–5.
101 Garth S J, 'Birefringence in bent single-mode fibers', *J. Lightwave Technol*., 1988, **6**(3), 445–9.
102 Sakai J I and Kimura T, 'Birefringence and polarization characteristics of single-mode optical fibers under elastic deformations', *IEEE J. Quantum Electron*., 1981, **17**(6), 1041–51.
103 Dai C, Yang D X, Tao X M et al., 'Effects of pure bending on the sensing characteristics of fiber Bragg gratings', In *Proc. SPIE – International Conference on Sensors and Control Techniques*, 2000, **4077**, 92–6.
104 Suhir E, 'Effect of the nonlinear stress–strain relationship on the maximum stress in silica fibers subjected to two-point bending', *Appl. Optics*, 1993, **32**(9), 1567–72.
105 Liu Y, Zhang L, Williams J A R et al., 'Optical bend sensor based on measurement of resonance mode splitting of long-period fiber grating', *IEEE Photon. Technol. Lett*., 2000, **12**(5), 531–3.
106 Ye C C, James S W and Tatam R P, 'Simultaneous temperature and bend sensing with long-period fiber gratings', *Optics Lett*., 2000, **25**(14), 1007–9.
107 Gander M J, MacPherson W N, McBride R et al., 'Bend measurement using Bragg gratings in multicore fibre', *Electron. Lett*., 2000, **36**(2), 120–1.